Journal of Inorganic Biochemistry 235 (2022) 111932

Contents lists available at ScienceDirect

Journal of Inorganic Biochemistry

journal homepage: www.elsevier.com/locate/jinorgbio

# Solution chemical properties and anticancer potential of 8-hydroxyquinoline hydrazones and their oxidovanadium(IV) complexes

Nádia Ribeiro [a,1], Ipek Bulut [b,1], Vivien Pósa [c], Baris Sergi [b], Giuseppe Sciortino [d], João Costa Pessoa [a], Luisa B. Maia [e], Valeria Ugone [f], Eugenio Garribba [g], Éva A. Enyedy [c], Ceyda Acilan [b,h,**], Isabel Correia [a,*]

[a] Centro de Química Estrutural, Institute of Molecular Sciences and Departamento de Engenharia Química, Instituto Superior Técnico, Universidade de Lisboa, Av. Rovisco Pais 1, 1049-001 Lisboa, Portugal
[b] Koç University, School of Medicine, Sariyer, Istanbul, Turkey
[c] MTA-SZTE Lendület Functional Metal Complexes Research Group, Department of Inorganic and Analytical Chemistry, University of Szeged, Dóm tér 7, H-6720 Szeged, Hungary
[d] Institute of Chemical Research of Catalonia (ICIQ), The Barcelona Institute of Science and Technology, Spain
[e] LAQV, REQUIMTE, NOVA School of Science and Technology | FCT NOVA, Campus de Caparica, 2829-516 Caparica, Portugal
[f] Istituto di Chimica Biomolecolare, Consiglio Nazionale delle Ricerche, Trav. La Crucca 3, I-07100 Sassari, Italy
[g] Dipartimento di Medicina, Chirurgia e Farmacia, Università di Sassari, Viale San Pietro, I-07100 Sassari, Italy
[h] Koç University, Research Center for Translational Medicine (KUTTAM), Istanbul, Turkey

ARTICLE INFO

*Keywords:*
Oxidovanadium(IV) complexes
8-hydroxyquinoline derivatives
Schiff bases
Solution stability
Speciation
Anticancer

ABSTRACT

We report the synthesis and characterization of a family of benzohydrazones ($L^n$, $n = 1$–6) derived from 2-carbaldehyde-8-hydroxyquinoline and benzylhydrazides containing different substituents in the *para* position. Their oxidovanadium(IV) complexes were prepared and compounds with 1:1 and 1:2 metal-to-ligand stoichiometry were obtained. All compounds were characterized by elemental analyses and mass spectrometry as well as FTIR, UV–visible absorption, NMR (ligand precursors) and EPR (complexes) spectroscopies, and by DFT computational methods. Proton dissociation constants, lipophilicity and solubility in aqueous media were determined for all ligand precursors. Complex formation with V(IV)O was evaluated by spectrophotometry for $L^4$ (Me-substituted) and $L^6$ (OH-substituted) and formation constants for mono $[VO(HL)]^+$, $[VO(L)]$ and bis $[VO(HL)_2]$, $[VO(HL)(L)]^-$, $[VO(L)_2]^{2-}$ complexes were determined. EPR spectroscopy indicates the formation of $[VO(HL)]^+$ and $[VO(HL)_2]$, with this latter being the major species at the physiological pH. Noteworthy, the EPR data suggest a different behaviour for $L^4$ and $L^6$, which confirm the results obtained in the solid state. The antiproliferative activity of all compounds was evaluated in malignant melanoma (A-375) and lung (A-549) cancer cells. All complexes show much higher activity on A-375 ($IC_{50} < 6.3$ μM) than in A-549 cells ($IC_{50} > 20$ μM). Complex **3** (F-substituted) shows the lowest $IC_{50}$ on both cell lines and lower than cisplatin (in A-375). Studies identified this compound as the one showing the highest increase in Annexin-V staining, caspase activity and induction of double stranded breaks, corroborating the cytotoxicity results. The mechanism of action of the complexes involves reactive oxygen species (ROS) induced DNA damage, and cell death by apoptosis.

## 1. Introduction

Cancer is a leading cause of death worldwide and the development of effective and safe treatments is crucial for improved clinical outcomes. Interest in antitumour metallodrugs stems from the remarkable anticancer effectiveness of cisplatin and related Pt-drugs, used in ~50% of all tumour chemotherapies and exhibiting activity against many types of solid tumours. However, severe toxicity and intrinsic or acquired resistance restrict the use of Pt-compounds. To overcome these limitations, other metallodrugs have been investigated, but only a small

* Corresponding author.
** Corresponding author at: Koc University, School of Medicine, SNA 261, Sariyer, Istanbul, Turkey.
*E-mail addresses:* cayhan@ku.edu.tr (C. Acilan), icorreia@tecnico.ulisboa.pt (I. Correia).
[1] These authors contributed equally to this work.

https://doi.org/10.1016/j.jinorgbio.2022.111932
Received 20 May 2022; Received in revised form 22 June 2022; Accepted 10 July 2022
Available online 15 July 2022

number of clinically useful compounds have been obtained.

The 8-hydroxyquinoline (8HQ) moiety is a privileged scaffold for drug development due to its wide range of potential therapeutic applications from which we highlight their antimicrobial [1], antitubercular [2], antifungal [3,4] and anticancer [5,6] activities. 8HQ derivatives are N,O-binding ligands, and display remarkable binding abilities, as well as interesting photophysical and pharmacological properties [4,7–10]. As examples, clioquinol (5-chloro-7-iodo-8-hydroxyquinoline) and nitroxoline (5-nitro-8-hydroxyquinoline) are two 8HQ-derived molecules used in the clinic. Clioquinol is an antifungal and antiprotozoal drug that has been restricted or discontinued in some countries due to its neurotoxic effects, while nitroxoline is used as a urinary antibacterial agent against Gram-positive and Gram-negative organisms [11]. Both compounds are currently under drug repurposing due to their wide spectrum of biological activity [12,13].

8-Hydroxyquinoline derivatives form stable complexes with different metal ions that also present interesting pharmacological profiles. Zinc(II) and copper(II) complexes of 5,7-dihalo-substituted-8-HQs showed high antiproliferative cytotoxicities against hepatoma (BEL-7404), ovarian (SK-OV-3) and non-small-cell lung (NCI-H460) human tumour cells, with $IC_{50}$ values from 1.4 nM to 32.13 μM [14]. Platinum (II) complexes of 8HQ and 2-methyl-8HQ exhibited enhanced cytotoxicity against hepatoma (BEL-7404 and Hep-G2), lung (NCI H460 and A559), and urinary bladder (T-24) tumour cells and low cytotoxicity on normal human liver HL-7702 cells. Both Pt-complexes were able to significantly reduce the mitochondrial membrane potential and increase the production of reactive oxygen species (ROS), as well as increase caspase-3/9 ratio in BEL-7404 cells [15].

The oxidovanadium(IV) complex of clioquinol, $[V(IV)O(clioquinolato)]_2$ was evaluated in human osteosarcoma cells, MG-63, showing enhanced antiproliferative activity ($IC_{50}$ = 7 μM at 24 h incubation *vs.* 59 μM for clioquinol) and selectivity towards bone cancer cells. Its effect on protein expression levels and inhibition of tyrosine phosphorylation showed that the compound can up-regulate proteins, such as caspases, and down-regulate others, such as poly (ADP-ribose) polymerase (PARP), involved in signalling pathways [16].

Fernandes and co-workers [17] reported on the antiproliferative action on colorectal (HCT116) and ovarian (A2780) cancer cells of oxidovanadium(V) complexes of the type $[V(V)O(OMe)(8HQ)_2]$, in which 8HQ are 8-hydroxyquinoline ligands with different substitution patterns. Overall, the cytotoxicity of the V(V)-complexes was higher than that of cisplatin, particularly in the ovarian cancer cell line, and most compounds showed low cytotoxicity to human primary fibroblasts. Additionally, the cell death mechanism, particularly in the ovarian cells, could be related to ROS generation. Complexes containing $V(IV)O^{2+}$ ions and 8HQ molecules substituted with methyl groups at positions 2-, 2,5- and 2,6- were also evaluated in the same cell lines, showing higher sensitivity for the colorectal cell line but no selectivity towards the selected cancer cells when compared to normal fibroblasts. The uptake of the complexes seemed to be associated with passive transport and the mechanism of cell death involved the production of intracellular ROS, triggering apoptosis and autophagy in the HCT116 cell line [18]. Several mixed ligand vanadium complexes containing 8HQ and derivatives depicted activity against *Mycobacterium tuberculosis* comparable or better than reference drugs such as streptomycin, as well as cytotoxic activity against cisplatin sensitive/resistant ovarian cells A-2780/A-2780cisR [19].

These studies clearly demonstrate the interest and relevance of vanadium complexes with 8HQ-derived ligands in the development of new anticancer drugs. However, new strategies in ligand design need to be developed and a promising approach is to modify the chelating ability via the introduction of additional donor groups, particularly if this occurs at position 2. Several 8HQ-thiosemicarbazone transition metal complexes have been designed taking advantage of this. A few Cu(II) complexes with this type of ligands showed strong anticancer activity against cisplatin-resistant neuroblastoma [20] and prostate cancer cells [21]. In addition, Cu(II)- and Zn(II)-8HQ thiosemicarbazone complexes were also prepared, with the Cu(II) analogues displaying cytostatic activity in different cancer cells, and the most active one showing $IC_{50} < 1$ μM [8].

An important class of compounds that has been gathering increasing attention for drug development are the hydrazide-hydrazone derivatives (that possess a -CO-NHN=CH- group) [22–27], since they hold a wide spectrum of bioactivity, including antibacterial, antitubercular, antifungal, anticancer and anti-inflammatory [28]. The condensation of 2-carbaldehyde-8-hydroxyquinoline with hydrazides is a suitable methodology to obtain hydrazide-hydrazone derivatives, which may be used to prepare new metal complexes. These compounds may coordinate transition metal ions in several ways, taking advantage of the increase in the number of donor groups when compared to 8HQ [29], leading to different properties. Schiff bases derived from 8-hydroxyquinoline-2-carboxaldehyde and aroylhydrazines fall in this category. The group of Zheng-Yin Yang first reported on these compounds in 2009, and used them to chelate rare earths ions, namely, Dy(III) [30], Eu(III) [31], Ho(III) [32], Nd(III) [33], Yb(III) [34], Er(III) [35], Tb(III) [36] and Sm(III) [37]. All compounds showed ability to bind DNA and displayed antioxidative properties. The authors claimed the compounds to be potential anticancer drugs, however no antiproliferative studies were done. To the best of our knowledge, no other complexes were reported containing these ligands.

The promising results obtained with vanadium complexes of 8HQ derivatives, and our interest in developing new metallodrugs based on oxidovanadium(IV) prompted us to prepare 8HQ Schiff base ligands and to use them to obtain new vanadium species with potential biological activity. Fig. 1 depicts the ligand precursors prepared, which were characterized in solution and solid state. $L^1$ and $L^6$ have been reported previously, while $L^2$ - $L^5$ and all V(IV)O-complexes prepared are new, to the best of our knowledge.

## 2. Experimental part

### 2.1. Materials and methods

Benzoic hydrazide (98%), 4-chlorobenzhydrazide (98%), 4-fluorobenzoic hydrazide (96%), 4-methoxybenzhydrazide (97%), and *p*-toluic hydrazide (99%) were all from Sigma-Aldrich, while 4-hydroxybenzhydrazide (*puriss*) was from Merck. Vanadyl acetylacetonate, $[V(IV)O(acac)_2]$, from Fluka was used as received. Dioxane (Fluka), methanol (Riedel-de-Haën) and ethanol (Fluka) were all p.a. grade and used without further purification.

4-(2-hydroxyethyl)-1-piperazineethanesulfonic acid (HEPES) was purchased from Sigma-Aldrich in *puriss* quality. Dimethyl sulfoxide (DMSO), $[V(IV)OSO_4]$, KCl, KOH, HCl and potassium hydrogen phthalate were obtained from Reanal (Hungary) and used without further purification. The V(IV)O stock solution was prepared as described in [38] and standardized for the metal ion concentration by permanganate

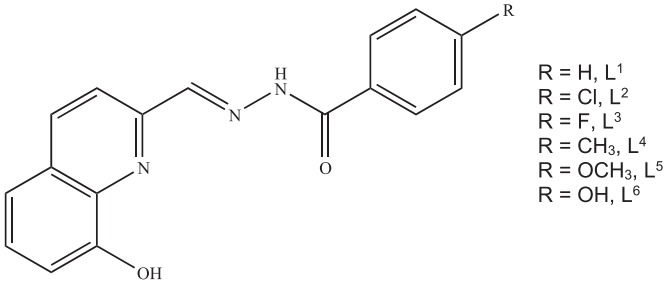


**Fig. 1.** Structural formula of the ligand precursors prepared, and abbreviations used. Abbreviations $L^1$ - $L^6$ represent globally all possible protonation forms of the compounds. Only when we want to specify a particular protonation form, the protons are included in the abbreviation.

titration. Milli-Q water was used for the preparation of all solutions.

UV–visible (UV–Vis) absorption spectra were recorded with a Perkin Elmer Lambda 35 spectrophotometer or a Agilent Cary 8454. Elemental analysis for C, H, N and S, were carried on a FISONS EA 1108 CHNS-O apparatus at *Laboratório de Análises do Instituto Superior Técnico*. $^{1}$H and $^{13}$C NMR spectra were recorded at ambient temperature on a Bruker Avance II + 300 (UltraShieldTM Magnet) spectrometer operating at 300 MHz for proton and at 75.4 MHz for carbon. The chemical shifts are reported in ppm using tetramethylsilane as internal reference. A JASCO FT/IR 4100 spectrophotometer was used for recording the infra-Red spectra and ESI-MS spectra of methanolic solutions of the compounds in both positive (+) and negative (−) modes were measured in a 500-MS Varian Ion Trap Mass Spectrometer.

### 2.2. Synthesis of the 8-hydroxyquinoline hydrazones ($L^1$–$L^6$)

2-Carbaldehyde-8-hydroxyquinoline was obtained by a mild oxidation of 2-methyl-8-hydroxyquinoline by refluxing it overnight with selenium dioxide in dioxane containing 2% water, as reported in the literature [39]. The isolation of the desired carbaldehyde was made by selective precipitation of the selenium impurities with an ethyl acetate/petroleum ether mixture, which afforded a clear yellow solution of the desired product. After solvent removal the aldehyde was obtained with enough purity to proceed to the following reactions.

The carbaldehyde (1.7 mmol) was dissolved in ca. 10 mL of methanol (MeOH) and stirred with a few drops of glacial acetic acid. The selected benzohydrazide (1.1 eq.) was added as a solid to the previous solution and left to reflux for 6 h, when a solid started to separate from the reaction mixture. After this, the mixture was allowed to cool to room temperature (RT) and then in the freezer for further precipitation. The solid product was finally collected by filtration, washed with ice-cold MeOH and dried under vacuum in a desiccator over silica-gel.

$L^1$: Light yellow solid. Yield: 73.4%. Elem. analysis for $C_{17}H_{13}N_3O_2{\cdot}0.1H_2O$ [found (calcd)]: C, 69.7% (70.09%); H, 4.5% (4.50%); N, 14.2% (14.42%). ESI-MS *m/z* (+) 292.18 (calcd for $[C_{17}H_{13}N_3O_2 + H]^+$ 292.12). FTIR (KBr pellet, cm$^{-1}$) 3359, 3319, 3051, 1687 (carbonyl), 1678 (quinol. C═N), 1547 (imine), 1266 (*δ*, CO phenol). UV–Vis [DMSO, λ, nm (ε, M$^{-1}$ cm$^{-1}$)] 264 (20880), 293 (shoulder, 48600), 303 (51000), 328 (31000), 337 (29000), 377 (shoulder, 5300). $^{1}$H NMR [300 MHz, DMSO_*d*$_6$, *δ* (ppm)]: 12.22 (1H, s, NH), 9.83 (1H, s, OH), 8.66 (1H, imine), 8.39–7.13 (10H, aromatic). $^{13}$C NMR [75.4 MHz, DMSO_*d*$_6$, *δ* (ppm)]: 163.5 (carbonyl), 147.7 (imine), 152.9–111.9 (aromatic).

$L^2$: Light yellow solid. Yield: 87.0%. Elem. analysis for $C_{17}H_{12}ClN_3O_2$ [found (calcd)]: C, 62.4% (62.68%); H, 3.6% (3.71%); N, 12.8% (12.90%). ESI-MS *m/z* (−) 324.32 (calcd for $[C_{17}H_{12}ClN_3O_2 - H]^-$ 324.05); (+) 326.09 (calcd for $[C_{17}H_{12}ClN_3O_2 + H]^+$ 326.07). FTIR (KBr pellet, cm$^{-1}$) 3417 (br), 3243 (m, sharp), 3186–3080 (aromatic CH), 1658 (carbonyl), 1651 (quinol. C═N), 1553 (imine). UV–Vis [DMSO, λ, nm (ε, M$^{-1}$ cm$^{-1}$)] 266 (18000), 296 (41000), 302 (42000), 336 (26000), 375 (5000). $^{1}$H NMR [300 MHz, DMSO_*d*$_6$, *δ* (ppm)]: 12.3 (1H, s, NH), 9.86 (1H, s, OH), 8.64 (1H, imine), 8.36–7.14 (9H, aromatic). $^{13}$C NMR [75.4 MHz, DMSO_*d*$_6$, *δ* (ppm)]: 161.8 (carbonyl), 148.2 (imine), 154.2–112.1 (aromatic).

$L^3$: Pale yellow solid. Yield: 87.0%. Elem. analysis for $C_{17}H_{12}FN_3O_2$ [found (calcd)]: C, 65.9% (66.02%); H, 3.8% (3.91%); N, 13.8% (13.59%). ESI-MS *m/z* (−) 308.33 (calcd for $[C_{17}H_{12}FN_3O_2 - H]^-$ 308.28); (+) 310.17 (calcd for $[C_{17}H_{12}FN_3O_2 + H]^+$ 310.30). FTIR (KBr pellet, cm$^{-1}$) 3401 (sharp, OH), 3212, 3041, 1653 (carbonyl), 1645 (quinol. C═N), 1559 (imine), 1506, 1465, 1286 (*δ*, CO phenol), 1234, 1154, 1099, 836, 762, 662 (aromatic F), 603. UV–Vis [DMSO, λ, nm (ε, M$^{-1}$ cm$^{-1}$)] 267 (15000), 297 (37000), 301 (38000), 330 (22000), 375 (4000). $^{1}$H NMR [300 MHz, DMSO_*d*$_6$, *δ* (ppm)]: 12.25 (1H, s, NH), 9.85 (1H, s, OH), 8.64 (1H, imine), 8.36–7.13 (9H, aromatic). $^{13}$C NMR [75.4 MHz, DMSO_*d*$_6$, *δ* (ppm)]: 162.5 (carbonyl), 148.0 (imine), 153.5–112.2 (aromatic).

$L^4$: Light yellow solid. Yield: 69.7%. Elem. analysis for $C_{18}H_{15}N_3O_2$ [found (calcd)]: C, 70.6% (70.81%); H, 4.8% (4.95%); N, 13.6% (13.76%). ESI-MS *m/z* (+) 306.09 (calcd for $[C_{18}H_{15}N_3O_2 + H]^+$ 306.13). FTIR (KBr pellet, cm$^{-1}$) 3386, 3284, 3050 (aromatic CH), 2919 (aliphatic CH), 1668 (carbonyl), 1634 (quinol. C═N), 1553 (imine). UV–Vis [DMSO, λ, nm (ε, M$^{-1}$ cm$^{-1}$)] 260 (20000), 300 (47000), 310 (50000), 350 (30000), 375 (5000). $^{1}$H NMR [300 MHz, DMSO_*d*$_6$, *δ* (ppm)]: 12.17 (1H, s, NH), 9.85 (1H, s, OH), 8.65 (1H, imine), 8.34–7.14 (9H, aromatic), 2.40 (3H). $^{13}$C NMR [75.4 MHz, DMSO_*d*$_6$, *δ* (ppm)]: 163.1 (carbonyl), 147.6 (imine), 152.5–112.1 (aromatic), 20.9 (methyl).

$L^5$: Pale yellow solid. Yield: 55.6%. Elem. analysis for $C_{18}H_{15}N_3O_3{\cdot}0.25H_2O$ [found (calcd)]: C, 66.0% (66.35%); H, 4.4% (4.79%); N, 12.8% (12.90%). ESI-MS *m/z* (−) 320.30 (calcd for $[C_{18}H_{15}N_3O_3 - H]^-$ 320.32); (+) 322.05 (calcd for $[C_{18}H_{15}N_3O_3 + H]^+$ 322.34). FTIR (KBr pellet, cm$^{-1}$) 3452, 3284, 3056, 2940, 1656 (carbonyl), 1645 (quinol. C═N), 1555 (imine), 1258–1178 (*δ*, CO phenol). UV–Vis [DMSO, λ, nm (ε, M$^{-1}$ cm$^{-1}$)] 260 (17000), 290 (37000), 305 (45000), 350 (28000), 370 (5000). $^{1}$H NMR [300 MHz, DMSO_*d*$_6$, *δ* (ppm)]: 12.12 (1H, s, NH), 9.83 (1H, s, OH), 8.64 (1H, imine), 8.34–7.10 (9H, aromatic), 3.85 (3H). $^{13}$C NMR [75.4 MHz, DMSO_*d*$_6$, *δ* (ppm)]: 163.0 (carbonyl), 147.2 (imine), 162.5–112.3 (aromatic), 55.1 (methoxy).

$L^6$: Light yellow solid. Yield: 75.4%. Elem. analysis for $C_{17}H_{13}N_3O_3$ [found (calcd)]: C, 66.0% (66.44%); H, 4.2% (4.26%); N, 13.5% (13.67%). ESI-MS *m/z* (−) 306.33 (calcd for $[C_{17}H_{13}N_3O_3 - H]^-$ 306.29); (+) 308.08 (calcd for $[C_{17}H_{13}N_3O_3 + H]^+$ 308.31). FTIR (KBr pellet, cm$^{-1}$) 3359, 3303, 3205, 1668 (carbonyl), 1657 (quinol. C═N), 1541 (imine), 1275–1224 (*δ*, CO phenol). UV–Vis [DMSO, λ, nm (ε, M$^{-1}$ cm$^{-1}$)] 263 (17000), 296 (shoulder, 27,500), 306 (30000), 340 (18500), 364 (shoulder, 9500). $^{1}$H NMR [300 MHz, DMSO_*d*$_6$, *δ* (ppm)]: trans isomer (15%): 15.67 (1H, s, NH), 10.85 (1H, s, OH, hydroxyquinoline), 10.26 (1H, s, OH, phenol), 7.83 (1H, imine), 8.54–6.96 (9H, aromatic cis isomer (85%): 12.03 (1H, s, NH), 9.82 (1H, s, OH, hydroxyquinoline), 10.20 (1H, s, OH, phenol), 8.62 (1H, imine), 8.33–6.90 (9H, aromatic). $^{13}$C NMR [75.4 MHz, DMSO_*d*$_6$, *δ* (ppm)]: trans isomer (15%): 160.9 (carbonyl), 137.2 (imine), 161.2–112.8 (aromatic) and cis isomer: 164.0 (carbonyl), 146.6 (imine), 161–112.1 (aromatic).

### 2.3. Synthesis of the oxidovanadium(IV) complexes

In a two-entry round bottom flask, 0.25 mmol of the corresponding ligand precursor were suspended in ca. 10 mL of previously degassed ethanol. The suspension was mantained under $N_2$ atmosphere while heating at 45 °C. In a separate flask, 0.25 mmol of [V(IV)O(acac)$_2$] were solubilized in ca. 10 mL of degassed ethanol and added to the previous hot suspension, while keeping the $N_2$ atmosphere. The green solution was left to reflux under the same conditions for 4 h. The final brown suspension was allowed to cool but filtered while still warm. The solid was washed with a cold ethanol:ethyl ether 1:1 mixture and dried under vacuum over silica-gel.

[VO($L^1$)] (**1**): Dark yellow solid. Yield: 43.0%. Elem. analysis for $C_{17}H_{11}N_3O_3V$ [found (calcd)]: C, 57.2% (57.32%); H, 3.3% (3.11%); N, 11.8% (11.80%). ESI-MS *m/z* (−) 372.21 (calcd for $[C_{17}H_{11}N_3O_3V^V + O]^-$ 372.02). FTIR (KBr pellet, cm$^{-1}$) 961 (*ν*, V=O). UV–Vis [DMSO, λ, nm (ε, M$^{-1}$ cm$^{-1}$)] 317 (30900), 366 (shoulder, 8300), 442 (2300).

[VO($L^2$)] (**2**): Dark yellow solid. Yield: 58.0 %. Elem. analysis for $C_{17}H_{10}ClN_3O_3V{\bullet}0.75H_2O$ [found (calcd)]: C, 50.7% (50.52%); H, 3.0% (2.87%); N, 10.2% (10.40%). ESI-MS *m/z* (−) 447.45 (calcd for $[C_{17}H_{11}N_3O_3V^V + O + CH_3CN]^-$ 447.73). FTIR (KBr pellet, cm$^{-1}$) 967 (*ν*, V=O). UV–Vis [DMSO, λ, nm (ε, M$^{-1}$ cm$^{-1}$)] 318 (32700), 365 (shoulder, 9600), 446 (2300).

[VO($HL^3$)$_2$] (**3**): Dark yellow solid. Yield: 34.5%. Elem. analysis for $C_{34}H_{22}F_2N_6O_5V{\bullet}H_2O$ [found (calcd)]: C, 58.0% (58.21%); H, 3.0% (3.45%); N, 11.8% (11.98%). ESI-MS *m/z* (+) 704.91 (calcd for $[C_{34}H_{22}F_2N_6O_5V + Na]^+$ 706.10). FTIR (KBr pellet, cm$^{-1}$) 982 (*ν*, V=O). UV–Vis [DMSO, λ, nm (ε, M$^{-1}$ cm$^{-1}$)] 319 (68000), 365 (shoulder,

19000), 443 (5400).

[VO($L^4$)] (**4**): Dark yellow solid. Yield: 44.0%. Elem. analysis for $C_{18}H_{13}N_3O_3V$•0.1$Et_2O$ [found (calcd)]: C, 58.9% (58.52%); H, 4.1% (3.74%); N, 11.4% (11.13%). ESI-MS *m/z* (−) 386.32 (calcd for $[C_{18}H_{13}N_3O_3V^V + O]^-$ 386.03). FTIR (KBr pellet, $cm^{-1}$) 1001 ($\nu$, V=O). UV–Vis [DMSO, λ, nm (ε, $M^{-1}$ $cm^{-1}$)] 323 (36900), 366 (shoulder, 10800), 441 (2700).

[VO($HL^5$)$_2$] (**5**): Dark yellow solid. Yield: 31.4%. Elem. analysis for $C_{36}H_{28}N_6O_7V$·2.25$H_2O$•0.75EtOH [found (calcd)]: C, 58.2% (58.33%); H, 4.8% (4.83%); N, 10.5% (10.88%). ESI-MS *m/z* (−) 723.40 (calcd for $[C_{36}H_{28}N_6O_7V^V + O]^-$ 723.14). FTIR (KBr pellet, $cm^{-1}$) 980 ($\nu$, V=O). UV–Vis [DMSO, λ, nm (ε, $M^{-1}$ $cm^{-1}$)] 309 (66500), 325 (70500), 367 (shoulder, 23000), 439 (5300).

[VO($HL^6$)$_2$] (**6**): Light brown solid. Yield: 30.7%. Elem. analysis for $C_{34}H_{24}N_6O_7V$ [found (calcd)]: C, 59.8% (60.10%); H, 3.8% (3.56%); N, 12.1% (12.37%). ESI-MS *m/z* (−) 695.15 (calcd for $[C_{34}H_{24}N_6O_7V^V + O]^-$ 695.11). FTIR (KBr pellet, $cm^{-1}$) 983 ($\nu$, V=O). UV–Vis [DMSO, λ, nm (ε, $M^{-1}$ $cm^{-1}$)] 308 (67500), 326 (63000), 368 (shoulder, 22000), 440 (3800).

### 2.4. UV–Vis spectrophotometric measurements, solubility and lipophilicity assays

An Agilent Cary 8454 diode array spectrophotometer was used to record the UV–Vis spectra in the range 200–800 nm. The path length was 1.0 cm and the temperature was 25.0 ± 0.1 °C. The UV–Vis spectrophotometric titrations were carried out using a Metrohm 665 Dosimat burette and an Orion 710A pH-meter equipped with a Metrohm combined electrode. Ionic strength of 0.10 M (KCl) was used in order to keep the activity coefficients constant. The titrations were performed with 0.10 M carbonate-free KOH solution with 30% (v/v) DMSO content. The electrode system was calibrated to the pH = −log[$H^+$] scale by means of blank titrations (HCl *vs.* KOH) according to the method of Irving *et al.* [40]. The average water ionization constant (p$K_w$) is 14.52 ± 0.05 in 30% (v/v) DMSO/water mixture. Argon was always passed over the solutions during the titrations, and the samples were deoxygenated before the titrations (for ~10 min). In the case of V(IV)O containing samples, argon overpressure was used when vanadium was added to the samples in tightly closed vessels, which were previously completely deoxygenated (for 20 min). Spectrophotometric titrations were carried out in 30% (v/v) DMSO/$H_2O$ on samples containing the ligand precursors at 50 or 60 μM concentration, in the pH range from 2.0 to 12.5 in the absence or in the presence of 1, 0.5 or 0.33 equiv. V(IV)O ions, using 10 mL sample volumes. Spectra were recorded between pH 1.5–2.0 using samples in which KCl was partially or completely replaced by HCl, and pH values were calculated from the strong acid concentration of the samples. Proton dissociation constants (p$K_a$) of the ligand precursors and overall stability constants of the complexes ($\beta$) were calculated by the computer program PSEQUAD [41] using literature data for V(IV)O hydroxido complexes: in particular, $[VO(OH)]^+$ (log$\beta$ = −5.94), $[(VO)_2(OH)_2]^{2+}$ (log$\beta$ = −6.95), $[(VO)_2(OH)_5]^-$ (log$\beta$ = −21.86), and $[(VO)(OH)_3]^-$ (log$\beta$ = −18.2) were considered [42–44]. It should be noted that the constants for these species are not known for the applied solvent mixture DMSO/$H_2O$.

To quantify the several V(IV)O-species, the usual definition of overall ($\beta$) and stepwise ($K$) formation constants is used:

$$\beta_{pqr} : pV^{IV}O^{2+} + qL + rH^+ \rightleftarrows \left[\left(V^{IV}O\right)_p(L)_q(H)_r\right]$$

$$\beta_{pqr} = \frac{\left[\left(V^{IV}O\right)_p(L)_q(H)_r\right]}{\left[\left(V^{IV}O\right)\right]^p[L]^q[H]^r}$$

$$\beta_n = \sum_{n=1}^{n=n} K_n$$

Thermodynamic solubility of the ligand precursors was measured for the saturated solutions in water at pH 7.40 (20 mM HEPES buffer) at 25.0 ± 0.1 °C. The concentration of the compounds was determined by UV–Vis spectrophotometry using stock solutions with known concentration dissolved in 100% DMSO, 50% and 10% (v/v) DMSO/buffered aqueous solutions for the calibration.

Distribution coefficient ($D_{7.4}$) values of selected ligand precursors were determined by shake-flask method in *n*-octanol/buffered aqueous solution at pH 7.40 in 20 mM HEPES buffer at 25.0 ± 0.2 °C. The compounds were dissolved at *ca.* 50 μM concentrations in *n*-octanol pre-saturated with the aqueous buffer. The stock solution in *n*-octanol was mixed with the buffer using 1:10 volume ratio using 360° vertical rotation for 3 h; then the samples were centrifuged at 5000 rpm for 5 min. The two phases were separated and their UV–Vis spectra were recorded. $D_{7.4}$ values were calculated from the absorbance values in the range of the $\lambda_{max}$ values ±10 nm ($D_{7.4} = A_o/((A_o^0\text{-}A_o) \times 10)$, where $A_o$ is the absorbance of the *n*-octanol phase after separation and $A_o^0$ is the absorbance of the original *n*-octanol stock solution).

### 2.5. EPR spectroscopy measurements

EPR spectra of the solid complexes **1**–**6** dissolved in DMSO were recorded using an X-band (9.4 GHz) Bruker EMX 6/1 spectrometer and a dual mode ER4116DM rectangular cavity (Bruker); samples were frozen in liquid nitrogen and spectra were acquired at *ca.* 100 K, with a modulation frequency of 100 kHz, modulation amplitude of 0.5 mT and microwave power of 635 μW.

EPR spectra in DMSO/$H_2O$ mixtures at different pH values were recorded at 120 K with an X-band (9.4 GHz) Bruker EMX spectrometer equipped with an HP 53150A microwave frequency counter. To increase the signal to noise ratio, signal averaging was used [45]. The microwave frequency to record the spectra was in the range 9.40–9.42 GHz, microwave power was 20 mW, the time constant was 163.8 ms, modulation frequency 100 kHz, modulation amplitude 4 G, sweep time 335.5 s, and the resolution 4096 points.

The solutions were prepared dissolving in mixtures DMSO/$H_2O$ 50/50 (v/v), 70/30 (v/v), 80/20 (v/v), a weighted amount of [V(IV)$OSO_4$]·3$H_2O$ and $L^4$ or $L^6$ to obtain a metal ion concentration of 1.0 mM and a metal to ligand molar ratio of 1:1. Argon was bubbled through the solutions to ensure the absence of oxygen and avoid the oxidation of $V(IV)O^{2+}$ ion. The pH values in the solvent mixtures were measured after calibrating the electrode with buffer solutions in the corresponding mixtures.

### 2.6. DFT calculations

The geometry of the isomers of $L^6$ and V(IV)O complexes formed by $L^6$ was optimized with Gaussian 16 software, rev B.01 [46] at DFT theory level using the hybrid B3LYP functional combined with Grimme's D3 correction [47] for dispersion and the split-valence plus polarization function 6-31 g(d,p) basis set for the main group elements, SDD plus *f*-functions (BS1) [48] and pseudopotential for vanadium. The effect of solvation was taken into account using the SMD continuum model of Marenich *et al.* [49]. Frequency calculations were carried out for all the optimized geometries in order to characterize the stationary points as either minima or transition states. It was confirmed that transition states connect with the corresponding intermediates by usual intrinsic reaction coordinate (IRC) calculations and subsequent optimization to minima. Final Gibbs energies were determined by adding the thermal and entropic corrections obtained with BS1 to the potential energies obtained with single point calculations using an extended basis set (BS2). BS2 consists in the triple-ζ def2-TZVP basis set for the main group elements and the quadruple-ζ def2-QZVP basis set for vanadium [50]. A correction of 1.9 kcal $mol^{-1}$ was applied to all Gibbs values to change the standard state from the gas phase (1 atm) to solution (1 M) at 298.15 K [51,52].

The $^{51}V$ hyperfine coupling tensor ***A*** of the V(IV)O-complexes was calculated with Gaussian 16 employing BHandHLYP functional and 6-

311+g(d) basis set [53–55]. For the 'bare' vanadium(IV) species formed by $L^4$, $[V(L^4)_2]$, the tensor ***A*** was predicted with ORCA software version 4.0 [56,57] using B2PLYP functional and VTZ basis set, as suggested previously [58]. The percent deviation (PD) of the absolute calculated value ($|A_z|^{calcd}$) from the absolute experimental value ($|A_z|^{exptl}$) was obtained as $100 \times [(|A_z|^{calcd} - |A_z|^{exptl})/|A_z|^{exptl}]$.

### 2.7. Agarose gel electrophoresis for complex/DNA interactions

Previously published protocols were followed with slight modifications [59]. Briefly, plasmid DNA (200 ng, pBOS-H2B-GFP, BD Biosciences) was incubated overnight at RT with complexes **1**–**6**, and cisplatin (200–400 μM, in 20 μL). For ROS scavenging activity, $NaN_3$ (final concentration 37.5 mM in doubly distilled $H_2O$) was added. Samples were run on a 1% agarose gel (100 V, 60 min). The experiments were carried out with two replicates, and band intensities were further quantified and analysed using ImageJ software.

### 2.8. Cell culture and cytotoxicity experiments

#### 2.8.1. Culture conditions

A-549 (ATCC, CCL-185) cells were grown in Dulbecco's Modified Eagle Medium F-12 (Gibco #11320033) and A-375 cells (ATCC, CRL-3222) were grown in Dulbecco's Modified Eagle Medium with high glucose (Gibco #11965118), supplemented with 10% FBS (Gibco, 10500064) and penicillin-streptomycin (10,000 U/mL, Gibco, 15140122). Cells were incubated at 37 °C, 5% $CO_2$ incubator and passaged every 2–3 days.

#### 2.8.2. Sulforhodamine B (SRB) assay

Stock solutions of all compounds were prepared in DMSO (10 mM), aliquots were stored at −20 °C, thawed on the day of the experiment and used only once. For SRB assay, $4 \times 10^3$ A-549 and A-375 cells were seeded on 96-well plates and treated with serial dilutions of indicated compounds (0–50 μM) for 72 h. Trichloroacetic acid (TCA) was added to wells at 10% final concentration, and cells were fixed (1 h, 4 °C). Then, each well was washed five times with $ddH_2O$, dried, and incubated with 4% (v/w) SRB dye (50 μL/well) for 30 min at RT. Following incubation, wells were washed with 1% acetic acid (v/v) five times, and 150 μL of 10 mM TRIS-base solution was added for even colour formation. Colorimetric measurements were performed at 564 nm wavelength reading. Viability percentage was calculated as follows: % Cell Viability = [100 × (Sample Abs-blank)/(Non-treated control Abs-blank)].

### 2.9. Flow cytometry analyses

$4 \times 10^4$ cells were seeded on 12-well plates and the next day cells were exposed to either vanadium complexes (calculated $IC_{70}$ values) or cisplatin (25 μM). Following 48 h of treatment, cells were trypsinized and resuspended in PBS solution supplemented with 1% FBS ($10^6$ cells/mL). The protocols below were followed for the described analyses.

#### 2.9.1. Annexin V staining

100 μL Cell suspension was mixed with Annexin V and 7-AAD solution in 1:1 ratio and incubated at RT for 20 min. Cells were counted with Muse Cell Analyzer (Merck Millipore).

#### 2.9.2. Caspase 3/7 staining

50 μL Cell suspension was mixed with 5 μL Caspase 3/7 antibody (1:8 diluted in PBS), and incubated at RT for 30 min. 150 μL of 7-AAD antibody mixture (1:75 diluted with 1 × Assay Buffer) was added to the cells and incubated at RT for 5 min. Apoptotic cells were counted using Muse Cell Analyzer (Merck Millipore).

#### 2.9.3. γH2AX staining

100 μL Cell suspension was mixed with 1 × fixation buffer in 1:1 ratio and incubated on ice for 5 min. Cells were centrifuged at 300 *g* for 5 min and the supernatant was discarded. The cell pellet was resuspended with 1 × permeabilization buffer and incubated on ice for 5 min. Cells were centrifuged at 300 *g, where g is the relative centrifugal force,* for 5 min and the supernatant was discarded. The cell pellet was resuspended with the 50 μL of antibody mixture. (20×) Anti-phospho-Histone H2A.X (Ser139), Alexa Fluor 555 and (20×) Anti-H2A.X, PECy5 antibodies were diluted with 1 × assay buffer. Following 30 min incubation on RT, cells were centrifuged and resuspended with 200 μL of 1 × assay buffer. Double stranded breaks were analysed with Muse Cell Analyzer (Merck Millipore).

#### 2.9.4. ROS activation

Oxidative stress reagent was diluted with 1 × assay buffer in 1:100 ratio. This medium solution was further diluted with 1 × assay buffer in (1:80 dilution) and oxidative stress working solution was prepared. 50 μL of cell suspension was mixed with 150 μL of working solution and incubated at 37 °C for 30 min. ROS (+) cells were analysed with Muse Cell Analyzer (Merck Millipore).

## 3. Results and discussion

### 3.1. Synthesis and characterization of the 8-hydroxyquinoline hydrazones

The ligand precursors were obtained through condensation of 2-carbaldehyde-8-hydroxyquinoline with benzohydrazines bearing different substituents in the *para* position of the hydrazide group. The substituents, having different electronic properties, are expected to influence the coordination to the metal center but can also be important in establishing interactions with biological molecules, considering their potential anticancer application. The desired products were obtained in good to excellent yields and the elemental analyses (CHN) and mass spectra (ESI-MS) were in very good agreement with the expected formulae, depicted in Fig. 1.

The organic compounds were further analysed through $^1H$ and $^{13}C$ NMR and the corresponding signals were all identified [see Experimental and Supplemental Material (SM)]. These compounds may show different isomers (cis/trans), regarding the orientation of the imine proton and the lone pair of electrons on the imine nitrogen. All compounds show only one isomer (cis), while $L^6$ shows the presence of 15% trans isomer (**Table S1**). The azomethine proton appears around 8.65 ppm for $L^1$– $L^5$, while for $L^6$ it is present at 8.62 ppm (cis) and 7.83 ppm (trans); the corresponding carbon atom is found between 147.2 and 148.2 ppm for the first five compounds, and at 146.6 ppm (cis) and 137.2 (trans) ppm for the last. All proton spectra present two downfield singlet peaks assigned to protons bound to the heteroatoms.

The FTIR spectra of the ligand precursors present characteristic bands for the functional groups found in these molecules (see Experimental and **Table S2**). The stretching vibrations for the OH, NH and aromatic CH appear in the region 3445–3040 $cm^{-1}$. The intense carbonyl stretching vibration is present between 1656 and 1687 $cm^{-1}$, while the $\nu$(C=N) is found between 1541 and 1559 $cm^{-1}$, both types of bands being sensitive to electronic effects.

The UV–Vis absorption spectra of DMSO solutions of these compounds present intense bands, with ε values in the order of $10^4$ $M^{-1}$ $cm^{-1}$ in the region 260–350 nm, characteristic for the $\pi \rightarrow \pi^*$ and $n \rightarrow \pi^*$ transitions within the different moieties of the compounds. The obtained data for these compounds are included in **Table S2** and are in good agreement with previously published structures, similar to those reported here [60,61].

Compounds containing imine bonds are susceptible to hydrolysis and thus the behaviour of the ligand precursors was evaluated in the mM concentration range by $^1H$ NMR spectroscopy. Solutions of each compound were prepared in DMSO_$d_6$ and $^1H$ NMR spectra were measured as aliquots of $D_2O$ were added (see **Fig. S1**) and also with increasing time

(up to 24 h). Although no hydrolysis products were found, precipitation was observed in the experiments revealing the low aqueous solubility of the compounds.

### 3.2. Proton dissociation processes, lipophilicity and solubility of the ligand precursors

The knowledge of the proton dissociation processes is important to predict the chemical form of a compound at a given pH value. Thus, the p$K_a$ values are key parameters as they affect the actual chemical charge, the lipophilic character and ultimately the pharmacokinetic properties. The p$K_a$ values of the ligand precursors were determined by UV–Vis spectrophotometric titrations using low concentrations (ca. 50–60 μM) in a 30% (v/v) DMSO/$H_2O$ solvent mixture, due to their low water solubility. The experimentally determined thermodynamic solubility ($S_{7.4}$) of the compounds in water at pH 7.4 and 25 °C is fairly low (< 4 μM; see $S_{7.4}$ values in Table 1). Representative UV–Vis spectra for $L^1$ and $L^6$, as well as the molar absorbance spectra of the species in the different protonation forms are shown in Figs. 2 and **S2**. The stock solutions of the ligand precursors were prepared in DMSO freshly every day. In this solvent all compounds are fairly soluble (mM range). The appearance of the isosbestic points in the spectra indicated that no measurable decomposition took place in the timeframe of the titrations; however, time-dependence studies revealed that these Schiff bases tend to hydrolyse slowly, especially at the highly basic pH range (**Fig. S3**).

Compounds $L^1$-$L^5$ possess three dissociable protons (OH, quinolinium $NH^+$ and benzohydrazide NH), while $L^6$ has an additional phenolic OH group which may dissociate. As all these functional groups are found at or nearby chromophoric moieties, their deprotonation is accompanied by significant spectral changes. However, in all cases only three p$K_a$ values could be calculated based on the spectra recorded in the pH range 1.5–12.5 (Table 1) (notably, due to the determined three p$K_a$ values, all ligand precursors are denoted as $H_3L^+$ in their completely protonated forms). The suggested deprotonation steps for $L^1$-$L^5$ are shown in Scheme 1. The most acidic p$K_a$ belongs to the quinolinium $NH^+$ group, while p$K_{a2}$ and p$K_{a3}$ to the hydroxyl and the benzohydrazide NH moieties, respectively. However, the proton dissociation processes of $H_2L$ and $HL^-$ are partly overlapped as the representative concentration distribution curves show for $L^1$ (Fig. 3**.a**). p$K_{a1}$ and p$K_{a2}$ of $L^1$-$L^5$ are much lower than those of 8-hydroxyquinoline under the same conditions (p$K_{a1}$ = 4.42, p$K_{a2}$ = 10.15 in 30% (v/v) DMSO/$H_2O$ [62]), especially the p$K_a$ of the quinolinium nitrogen that is affected by the neighbouring benzohydrazide moiety. Based on the obtained p$K_a$ values, ligands $L^1$-$L^5$ are present in solution in their neutral $H_2L$ form at physiological pH.

Considering this set of compounds, it can be concluded that the effect of the various aromatic ring substituents on the p$K_a$ of OH and $NH^+$ moieties of the 8-hydroxyquinoline part is minimal. While the electron withdrawing chlorine and fluorine substituents decrease the p$K_a$ of the benzohydrazide-NH, the electron donating methyl and methoxyl groups increase it.

$L^6$ behaves somewhat differently in the basic pH range as most probably the phenolic OH also deprotonates in an overlapping process with the hydroxyl of the 8-hydroxyquinoline scaffold (see the suggested deprotonation steps in **Scheme S1**). As a result, p$K_{a2}$ = 8.29 was obtained for $L^6$, while p$K_{a3}$ remains similar to the p$K_a$ value (p$K_{a2}$) of the OH group of the other compounds, although the deprotonation of the two OH moieties overlaps (Fig. 3**.b**). The p$K_a$ of the benzohydrazide-NH moiety for $L^6$ could not be determined accurately, since its dissociation takes place in the fairly basic pH range; most likely the phenolate increased this p$K_a$ due to its electron donating and mesomeric effects. These conclusions were also corroborated at the mM range in an experiment followed through $^1$H NMR spectroscopy (see **Fig. S4** with explanation). Based on the p$K_a$ values, in the case of $L^6$, the fraction of the neutral $H_2L$ is 88% at pH 7.4, and 12% is the monoanionic $HL^-$ form due to the deprotonation of the phenolic OH (Fig. 3**.b**). However, this difference in the charges between the two groups of the compounds ($L^1$-$L^5$*vs.* $L^6$) at pH 7.4 did not bring significant differences in the solubility (Table 1). Notably, the compounds with the chlorine and fluorine substituents were found to be less soluble in comparison to the other ligands.

The distribution coefficients of the studied compounds were determined at pH 7.4 via the partitioning between *n*-octanol and water (see $D_{7.4}$ values in Table 1). The compounds are fairly lipophilic and the presence of all the substituents (mainly the methoxy) increased the lipophilicity at the physiological pH when compared to the reference compound $L^1$.

### 3.3. Synthesis and characterization of the oxidovanadium(IV) complexes

Although the complexation reactions were all done under the same reaction conditions, namely with a 1:1 stoichiometric ratio of ligand precursor and metal ion, two different types of vanadium complexes were obtained. Elemental analyses of the dark yellow solids that precipitated from the reaction media indicated a 1:1 L:M stoichiometry for complexes obtained with $L^1$, $L^2$ and $L^4$, and 2:1 for complexes from $L^3$, $L^5$ and $L^6$. These assignments were further corroborated by ESI-MS results. In the FTIR spectra (**Table S2**) all complexes show a new band appearing in the range 961–1000 $cm^{-1}$ evidencing the presence of the V=O group [19,63–65]. The spectra present broad bands around 3450 $cm^{-1}$ indicating the existence of water or solvent molecules in the solids. The band associated with the vibration of C=N in the quinoline ring decreases >20 $cm^{-1}$ when compared to the free ligands, evidencing the coordination of the nitrogen to vanadium.

The UV–Vis absorption spectra of the complexes in DMSO solutions (**Table S2**) present the characteristic bands for the intraligand transitions and less intense bands, with ε in the order of $10^3$ $M^{-1}$ $cm^{-1}$, centred at 442 nm, associated to charge transfer between the organic compound and the oxidovanadium(IV) center. No d-d bands could be detected due to their low molar absorptivity.

The paramagnetic complexes were characterized in DMSO solution by EPR spectroscopy. Fig. 4 shows the measured spectra (at ~100 K), as well as the simulation obtained for the spectra of $[VO(HL^6)_2]$ with the program developed by Rockenbauer and Korecz [66]. The experimental spectra exhibit hyperfine patterns consistent with axial-type spectra of V(IV)O species with a $d^1_{xy}$ ground state. The broadening of the spectral bands indicates that the compounds aggregate to some extent in this

**Table 1**
p$K_a$ values of the studied ligand precursors determined by UV–Vis spectrophotometric titrations in 30% (v/v) DMSO/$H_2O$ in addition to their thermodynamic solubility ($S_{7.4}$) and distribution coefficients (log$D_{7.4}$) at pH 7.40 determined experimentally via *n*-octanol/water partitioning. *[t = 25 °C; I = 0.1 M (KCl)].*

| | $L^1$ | $L^2$ | $L^3$ | $L^4$ | $L^5$ | $L^6$ |
|---|---|---|---|---|---|---|
| R = | H | Cl | F | $CH_3$ | $OCH_3$ | OH |
| p$K_{a1}$ | 2.24 ± 0.03 | 2.11 ± 0.01 | 2.10 ± 0.03 | 2.18 ± 0.03 | 2.34 ± 0.03 | 2.33 ± 0.03 |
| p$K_{a2}$ | 9.51 ± 0.03 | 9.39 ± 0.03 | 9.45 ± 0.03 | 9.61 ± 0.03 | 9.61 ± 0.03 | 8.29 ± 0.03 |
| p$K_{a3}$ | 11.45 ± 0.03 | 11.01 ± 0.03 | 11.18 ± 0.03 | 11.67 ± 0.03 | 11.71 ± 0.03 | 9.65 ± 0.03 |
| p$K_{a4}$ | – | – | – | – | – | > 12 |
| $S_{7.4}$ (μM) | 3.7 | < 1 | < 1 | 1.7 | 2.0 | 2.1 |
| log$D_{7.4}$ | +1.49 ± 0.01 | +1.77 ± 0.02 | +1.70 ± 0.09 | +1.9 ± 0.1 | >2 | +1.85 ± 0.09 |

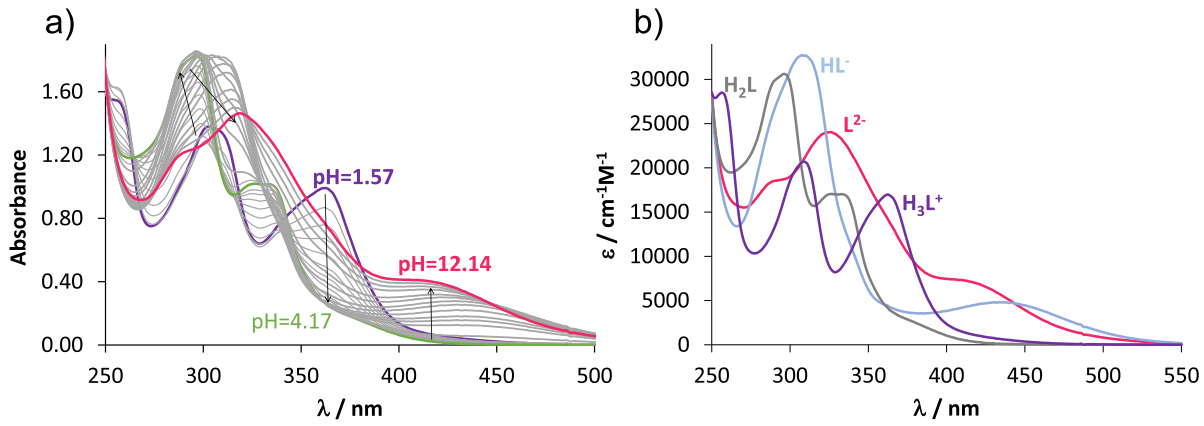


**Fig. 2.** a) UV–Vis spectra of $L^1$ recorded at various pH values and b) calculated individual absorption spectra of species in the different protonation states. *[$c_L$ = 60 μM; pH = 1.5–12.5; t = 25 °C; I = 0.10 M (KCl); ℓ = 1.0 cm; 30% (v/v) DMSO/$H_2O$].*

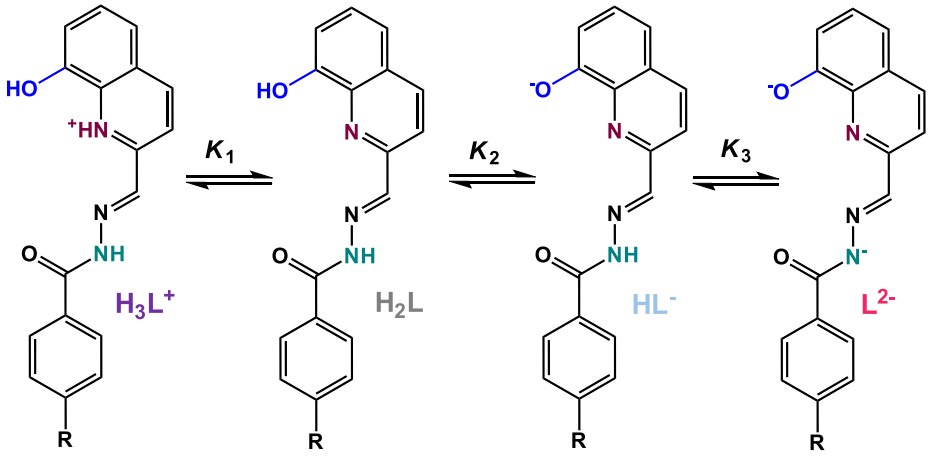


**Scheme 1.** Deprotonation steps of the compounds where R = H, Cl, F, $CH_3$, $OCH_3$. Notably, the proton dissociation processes of the OH and benzohydrazide NH moieties overlap (see Fig. 3.a), thus $K_2$ and $K_3$ do not belong only to the denoted groups.

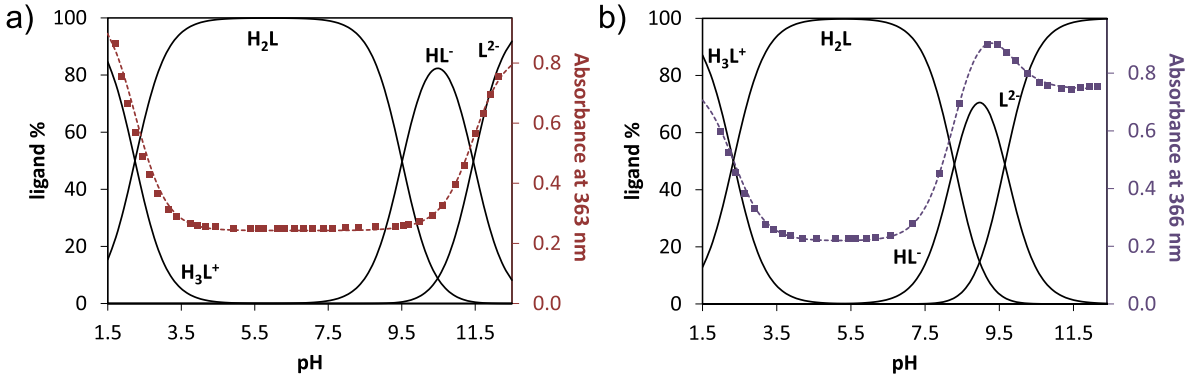


**Fig. 3.** Concentration distribution curves for a) $L^1$ and b) $L^6$ together with the measured (■) and fitted absorbance values at 363 nm ($L^1$) and 366 nm ($L^6$) at the different pH values. *[$c_L$ = 60 μM; t = 25 °C; I = 0.10 M (KCl); ℓ = 1.0 cm; 30% (v/v) DMSO/$H_2O$].*

solvent and at the applied temperature.

The quality presented by the EPR spectrum of $[VO(HL^6)_2]$ is sufficient to run its simulation and the obtained parameters were then used to help simulate the other spectra. The spin Hamiltonian parameters are shown in Table 2.

In the case of 1:1 complexes bearing only one ligand molecule (**1**, **2** and **4**), we expect the –NH–CO– group to deprotonate and the ligand to bind in a tri- or tetradentate mode to the metal centre. The experimental $|A_z|$ is in the range 164.8–165.7 × $10^{-4}$ $cm^{-1}$. Based on the DFT calculations (see *infra*), the EPR data are compatible with a tridentate dianionic binding mode for the ligand involving the donor set [($O^-$,N, $N^2_{im}$); DMSO]; for example, $|A_z^{calcd}|$ for [VO(L)] complex with $(L^6)^{2-}$

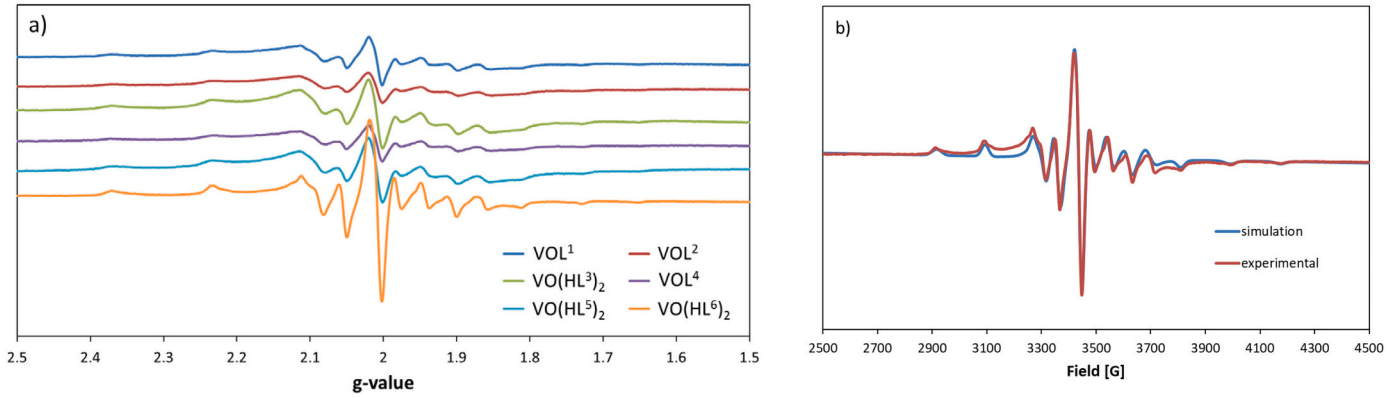


**Fig. 4.** a) First derivative X-band EPR spectra recorded at *ca.* 100 K in DMSO solution of the V(IV)O complexes. b) First derivative X-band EPR spectrum for [VO($HL^6$)$_2$] (**6**) in DMSO at *ca.* 100 K and its simulation.

**Table 2**
Spin Hamiltonian parameters calculated for the V(IV)O-complexes and proposed coordination equatorial plane.

| | $g_{x,y}$ | $\|A_{x,y}\|^a$ | $g_z$ | $\|A_z\|^a$ | Donor set |
|---|---|---|---|---|---|
| [VO($L^1$)] **(1)** | 1.982 | 52.1 | 1.952 | 165.6 | ($O^-$,N,$N^2_{im}$); DMSO |
| [VO($L^2$)] **(2)** | 1.979 | 52.5 | 1.953 | 165.7 | ($O^-$,N,$N^2_{im}$); DMSO |
| [VO($HL^3$)$_2$] **(3)** | 1.981 | 56.0 | 1.948 | 163.7 | ($O^-$,N); ($O^-$,$N^{ax}$); DMSO |
| [VO($L^4$)] **(4)** | 1.984 | 52.3 | 1.950 | 164.8 | ($O^-$,N,$N^2_{im}$); DMSO |
| [VO($HL^5$)$_2$] **(5)** | 1.981 | 56.4 | 1.946 | 164.0 | ($O^-$,N); ($O^-$,$N^{ax}$); DMSO |
| [VO($HL^6$)$_2$] **(6)** | 1.982 | 55.2 | 1.948 | 163.4 | ($O^-$,N); ($O^-$,$N^{ax}$); DMSO |

[a] $A_{xyz}$ in $10^{-4}$ $cm^{-1}$ units.

ligand is 166.9 × $10^{-4}$ $cm^{-1}$.

In contrast, for the [VO(HL)$_2$] complexes (**3**, **5** and **6**) $|A_z|$ is between 163.4 and 164.0 × $10^{-4}$ $cm^{-1}$ and the coordination sphere should involve [($O^-$,N); ($O^-$,$N_{ax}$); DMSO]. In particular, with $L^6$, the latter is the most stable isomer with $|A_z^{calcd}|$ (161.2 × $10^{-4}$ $cm^{-1}$) lower than that of the [VO(L)] complexes. Its binding mode is the same as for the species of V(IV)O with 8HQ and 8-hydroxyquinoline-5-sulfonate (HQS) [65] that show a *cis*-octahedral geometry with [($O^-$,N); ($O^-$,$N_{ax}$); $H_2O$] binding mode (see *infra*).

Considering all the data, the proposed formulae for these oxidovanadium(IV) complexes are presented in Scheme 2.

[VO($HL^5$)$_2$] (**5**) was tested for its resistance to oxidation by following its $^{51}$V NMR spectrum with time, as showed in **Fig. S5**. The complex solution was prepared in a mixture of 40% (v/v) $D_2O$/DMSO-$d_6$ and a very slow oxidation process was observed with a small broad vanadium (V) signal appearing at −520 ppm after one month, due to the presence of decavanadate oligomers. The sharp peak observed since the beginning of the experiment at *ca.* −550 ppm should be due to monomeric $HVO_4^{2-}$/$H_2VO_4^-$ species.

### 3.4. Stability of the oxidovanadium(IV) complexes in solution

Compounds $L^4$ and $L^6$ were selected for studying their complex formation with V(IV)O ions, and the stoichiometry and overall stability constants of the V(IV)O-complexes were determined by UV–Vis spectrophotometric titrations in 30% (v/v) DMSO/$H_2O$. Representative UV–Vis spectra are shown in Fig. 5.**a** for the V(IV)O-$L^6$ system. Comparing the spectra recorded in the absence and in the presence of the metal ion, it can be concluded that with both ligands the complexation starts already at acidic pH values.

Under the used conditions, stability constants for mono and bis V(IV)O-complexes ([VO(HL)]$^+$, [VO(L)], and [VO(HL)$_2$], [VO(HL)(L)]$^-$ and [VO(L)$_2$]$^{2-}$) could be determined (Table 3) by the deconvolution of the spectra. The molar absorbance spectra for these species in the case of $L^6$ are depicted in Fig. 5.**b**. Both EPR and DFT studies, carried out in these systems to help assigning the binding modes of the formed species (see *infra*), suggest that $L^4$ and $L^6$ behave differently. In the [VO(L)] and [VO(L)$_2$]$^{2-}$ complexes of $L^4$ the ligand is completely deprotonated ($L^{2-}$) suggesting the simultaneous coordination of the three potential donor atoms ($O^-$,N,$N^2_{im}$) at least for one of the two ligands (see 1:1 species in Scheme 2). For $L^6$ the formation energies computed at DFT level studies indicate that this tridentate coordination is not favourable; however, in this case, $L^{2-}$ denotes the presence of the deprotonated quinoline nitrogen and the two phenolates, while the benzohydrazide NH is assumed to be still protonated (see **Scheme S1**). Thus, these species of $L^6$ containing coordinated $L^{2-}$ should involve an 8HQ-type binding through ($O^-$,N) and ($O^-$,N); ($O^-$,$N_{ax}$); $H_2O$, respectively (with the two negative charges in $L^{2-}$ on the phenolato oxygens), with the formation of mixed hydroxido species with the binding of $OH^-$ ion being also possible.

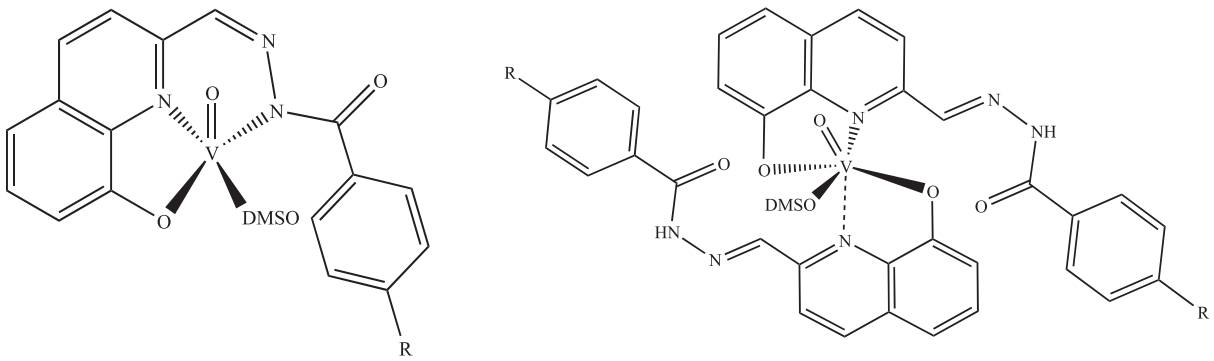


**Scheme 2.** Proposed formulae for the V(IV)O-complexes. The left structure represents the 1:1 complexes where R = H, Cl and $CH_3$; the structure on the right represents the 2:1 complexes where R = F, OH and $OCH_3$.

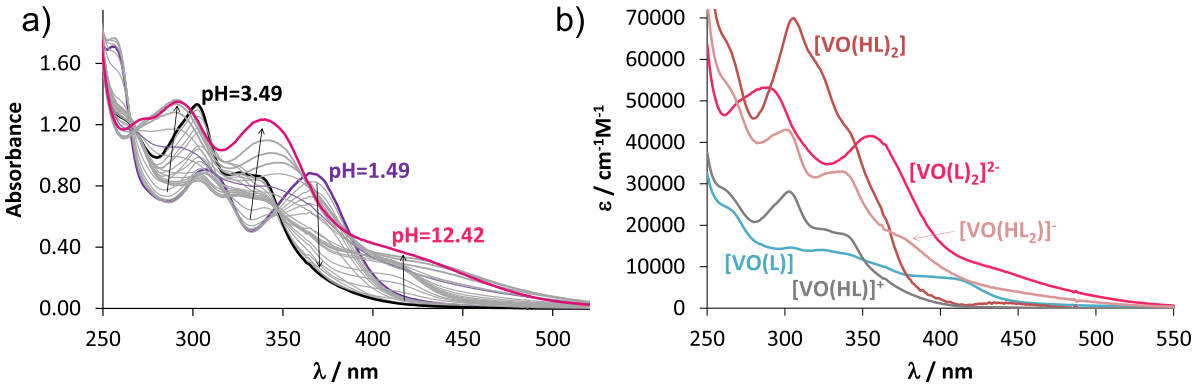


**Fig. 5.** a) UV–Vis spectra of the oxidovanadium(IV) – $L^6$ (1:1) system recorded at various pH values, and b) calculated individual molar absorption spectra of the complexes. $[VO(HL_2)]^-$ corresponds to $[VO(HL)(L)]^-$. *[$c_{V(IV)O}$= $c_L$= 50 μM; pH = 1.5–12.5; t = 25 °C; I = 0.10 M (KCl); ℓ (optical path) = 1.0 cm; 30% (v/v) DMSO/$H_2O$]*.

**Table 3**
Overall (log$\beta$), stepwise (log$K$) stability constants for the oxidovanadium(IV) complexes formed with $L^4$ and $L^6$ and p$K_a$ values of the protonated complexes determined by UV–Vis spectrophotometric titrations. *[t = 25.0 °C; I = 0.10 M (KCl); 30% (v/v) DMSO/$H_2O$]*.

| | $L^4$ | $L^6$ |
|---|---|---|
| R = | $CH_3$ | OH |
| log$\beta$ $[VO(LH)]^+$ | 23.11 ± 0.02 | 19.94 ± 0.02 |
| log$\beta$ [VO(L)] | 17.66 ± 0.02 | 14.57 ± 0.02 |
| log$\beta$ $[VO(HL)_2]$ | – | 36.77 ± 0.11 |
| log$\beta$ $[VO(HL)(L)]^-$ | 34.98 ± 0.07 | 29.48 ± 0.07 |
| log$\beta$ $[VO(L)_2]^{2-}$ | 26.06 ± 0.04 | 20.92 ± 0.08 |
| p$K_a$ $[VO(LH)]^+$ | 5.45 | 5.37 |
| p$K_a$ $[VO(HL)_2]$ | – | 7.29 |
| p$K_a$ $[VO(HL)(L)]^-$ | 8.92 | 8.56 |
| log$K$ $[VO(L)_2]^{2-}$ | 8.14 | 6.35 |

Complexes $[VO(HL)]^+$ with $L^4$ and $L^6$ are protonated mono-ligand species in which ($O^-$,N) coordination is also assumed. For the protonated bis complexes we could also determine stability constants (except for $[VO(HL^4)_2]$). In these species the binding via the ($O^-$,N) donor set is the most likely. Since in the spectrophotometric titrations the bands used for the calculations are ligand-based and charge transfers, thus less sensitive to metal coordination than d-d bands), EPR spectroscopy can strongly contribute to reveal the actual coordination modes.

Concentration distribution diagrams were calculated using the determined stability constants for both studied systems (Figs. 6 and **S6**).

The mono complexes predominate in a wider pH range (3.5–7.5) in both systems, while the fraction of the bis complexes is somewhat lower. The unfavourable coordination of the second ligand is also reflected in the stepwise stability constants, as log$K_2$ $[VO(L)_2]^{2-}$ is much lower than log$K_1$ [VO(L)] (Table 3). The overall stability constants are greater for $L^4$ than for $L^6$, however, the basicity of the ligands is different, so the constants cannot be compared directly. Comparing the fractions of the metal complexes and the unbound ligands in Fig. 6, it can be concluded that $L^6$ is a somewhat more efficient oxidovanadium(IV) binder at pH 7.4, while in the basic pH range $L^4$ seems to be a stronger binder.

To elucidate the coordination modes of the complexes and confirm the speciation model obtained by the UV–Vis titrations, EPR spectra were recorded at various pH values.

### 3.5. Coordination modes of the ligands

The coordination modes of the ligands depend on their conformation. In structure (**a**) (Scheme 3), the ligand can bind a metal ion only via the ($O^-$,N) donor set followed by the deprotonation of phenolic OH. The rotation around the C—C bond results in structure (**b**, trans orientation of the hydrogen atom and lone electron pair on the C=N) in which the metal may coordinate in a tetradentate mode with the donor set ($O^-$,N, $N^1_{im}$,CO) with the ligand singly or doubly deprotonated. An additional rotation around the C=N bond produces the form (**c**, cis orientation) which can bind the metal in a tridentate mode with the coordination ($O^-$,N,$N^2_{im}$) upon the deprotonation of OH and benzohydrazide-NH groups.

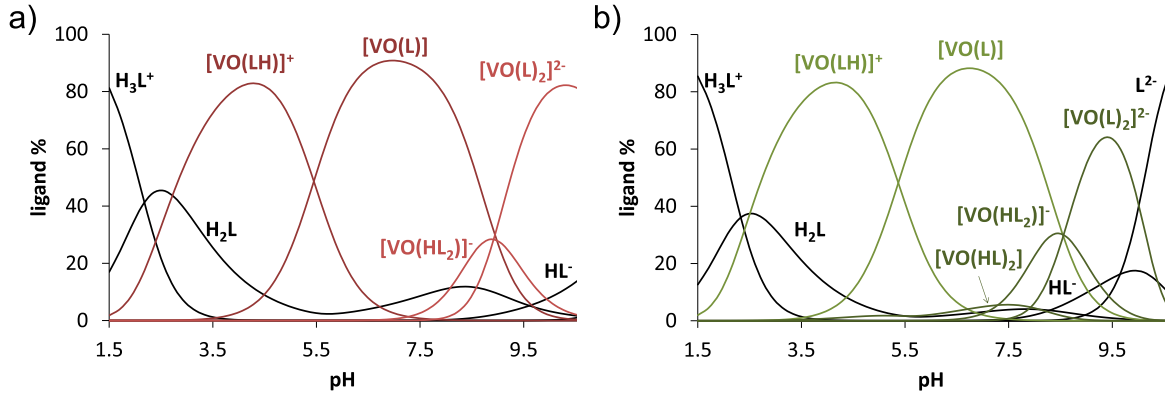


**Fig. 6.** Concentration distribution curves for a) oxidovanadium(IV)–$L^4$ (1:1) and b) oxovanadium(IV)–$L^6$ (1:1) systems. –$[VO(HL_2)]^-$ corresponds to $[VO(HL)(L)]^-$. *[$c_{V(IV)O}$= $c_L$= 50 μM; t = 25 °C; I = 0.10 M (KCl); 30% (v/v) DMSO/$H_2O$]*.

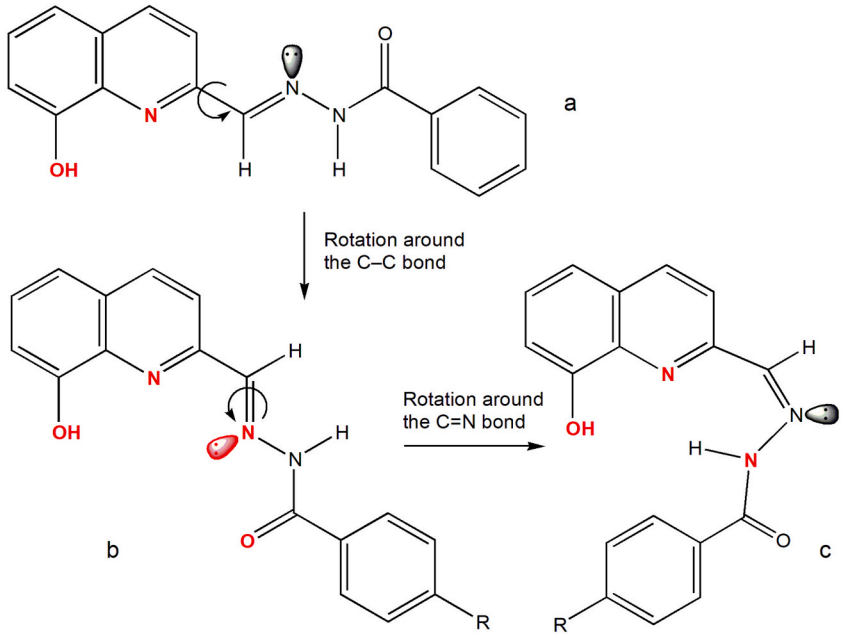


**Scheme 3.** The possible isomerization of **L** ligand precursor depending on the rotation around the C—C and C═N bonds.

The isomerization of the neutral ligand $L^6$ was examined, computing the Gibbs energy values at B3LYP-D3/BS2 in SMD continuum model for water [49]. The results show that the rotation around the C—C bond is possible at room temperature, with an energy barrier of 7.6 kcal $mol^{-1}$, while the rotation around the C═N bond is hindered displaying an energy barrier higher than 50 kcal $mol^{-1}$ (**Scheme S2**). This indicates that the structure and coordination mode of the V(IV)O-complexes would depend on the initial conformation of the ligands and could be a possible explanation for the different behaviour of these ligands (for example, $L^4$ and $L^6$). Notably, NMR studies corroborate the theoretical studies since only for $L^6$ cis and trans isomer were found (see **Table S1**), while for all other ligands only the cis isomer was obsereved.

### 3.6. EPR spectroscopy and DFT calculations

The anisotropic EPR spectra were recorded on the systems with $L^4$ and $L^6$ using various mixtures of DMSO/$H_2O$, containing increasing percentages of DMSO to favour the dissolution of the ligand and complexes and improve the resolution of the signals. The ratios DMSO/$H_2O$ (v/v) were 50/50, 70/30 and 80/20. In the spectrophotometric titrations performed at 25 °C the concentrations were much lower (50–60 uM) than in the EPR measurements in which 1.0 mM was the concentration required to obtain spectra with adequate resolution and intensity. Additionally, some differences may arise due to the pH values, despite the measurements having been made after calibrating the electrode with buffer solutions in the DMSO/$H_2O$ mixtures.

The spectra collected in the systems with $L^6$ with ratio DMSO/$H_2O$ 80/20 (v/v) are shown in Fig. 7, while the spin Hamiltonian parameters are listed in Table 4. With varying the pH, several species are formed in solution (their $M_I = 7/2$ resonances are indicated with **I-IV**). To characterize the compounds, DFT calculations in the framework of the SMD model were carried out. In particular, the structure of the V(IV) complexes was optimized, and $\Delta G_{aq}$ of formation and $^{51}V$ hyperfine coupling constants were calculated according to the methods established in the literature [53,54,67,68]. The structure of the examined species along with the predicted $\Delta G_{aq}$ and $A_z(^{51}V)$ are shown in Fig. 9**.** In the acidic pH range, after the aquation, two species with 1:1 composition denoted with **I** and **II** are formed. **I** is the 1:1 complex with mono-chelated coordination via (N,$O^-$) donor set of 8-hydroxyquinoline moiety; it has $g_z = 1.939$ and $|A_z| = 170.9 \times 10^{-4}$ $cm^{-1}$. To this species the stoichiometry

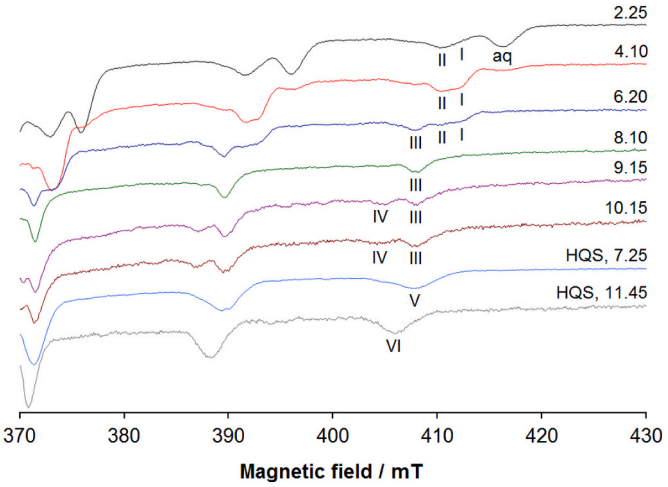


**Fig. 7.** High field region of the X-band anisotropic EPR spectra recorded as a function of pH at 120 K in a mixture DMSO/$H_2O$ 80/20 (v/v) containing $VOSO_4{\cdot}3H_2O$ and $L^6$ (molar ratio 1:1 and V(IV)O concentration 1.0 mM). With **I**, **II**, **III**, **IV**, **V** and **VI** the $M_I = 7/2$ resonances of $[VO(HL^6)]^+$, $[VO(H_2L^6)]^{2+}$, $[VO(HL^6)_2]/[VO(HL^6)(L^6)]^-$ with coordination ($O^-$,N); ($O^-$,$N_{ax}$); $H_2O$ plus ($O^-$, N); ($O^-_{ax}$,N); $H_2O$, $[VO(HL^6)(L^6)(OH)]^{2-}$, $[VO(HQS)_2(H_2O)]^{2-}$ and $[VO(HQS)_2(OH)]^{3-}$ species are indicated. HQS denotes 8-hydroxyquinoline-5-sulfonato ligand.

$[VO(HL^6)]^+$ can be assigned. The calculated values of $\Delta G_{aq}^{calcd}$ and $A_z^{calcd}$ are −13.6 kcal $mol^{-1}$ and − 169.5 × $10^{-4}$ $cm^{-1}$; $A_z^{calcd}$ agrees well with the data in the literature which suggest that the level of theory used in this study (BHandHLYP/6-311+g(d)) slightly underestimates the hyperfine coupling constant [53]. In the same pH range, another species (**II**) is formed with $g_z = 1.944$ and $|A_z| = 168.1 \times 10^{-4}$ $cm^{-1}$; for it, the coordination mode ($N^1_{im}$,CO) with a 5-membered cycle is expected and the stoichiometry should be $[VO(H_2L^6)]^{2+}$. Notably, these complexes were indistinguishable by UV–Vis spectrophotometry under the conditions used.

With increasing pH, species **III** with $g_z = 1.948$ and $|A_z| = 164.1 \times 10^{-4}$ $cm^{-1}$ is formed. Its parameters are very similar to the bis-chelated complexes of 8HQ ($g_z = 1.946$ and $|A_z| = 163 \times 10^{-4}$ $cm^{-1}$ [65]) and the

**Table 4**
Experimental spin Hamiltonian parameters of the V(IV) complexes formed by $L^4$ and $L^6$ ligands.

| | $L^6$ | | $L^4$ | | |
|---|---|---|---|---|---|
| Complex | $g_z$ | $\|A_z\|^a$ | $g_z$ | $\|A_z\|^a$ | Coordination mode |
| $[VO(H_2L)]^{2+}$ | 1.944 | 168.1 | 1.944 | 168.2 | $(N^1_{im},CO)$ |
| $[VO(HL)]^+$ | 1.939 | 170.9 | 1.941 | 170.2 | $(O^-,N)$ |
| $[VO(HL)_2]/[VO(HL)(L)]^{-b}$ | 1.948 | 164.1 | 1.948 | 164.2 | $(O^-,N)$; $(O^-,N_{ax})$; $H_2O$ |
| $[VO(HL)_2]/[VO(HL)(L)]^{-c}$ | 1.946 | ~167 | 1.946 | ~168 | $(O^-,N)$; $(O^-_{ax},N)$; $H_2O$ |
| $[VO(HL)(L)(OH)]^{2-d}$ | 1.954 | 157.3 | – | – | $(O^-,N)$; $(O^-,N_{ax})$; $OH^-$ |
| $[VO(L)]$ | – | – | 1.944 | 167.1 | $(O^-,N,N^2_{im})$; $H_2O$ |
| $[VL_2]$ | – | – | 1.931 | 128.8 | $2\times(O^-,N,N^2_{im})$ |

[a] Values in $10^{-4}$ $cm^{-1}$.
[b] Major isomer with coordination $(O^-,N)$; $(O^-,N_{ax})$; $H_2O$.
[c] Minor isomer with coordination $(O^-,N)$; $(O^-_{ax},N)$; $H_2O$.
[d] Mono-hydroxido complex with composition $[VO(HL)(L)(OH)]^{2-}$.

sulfonate derivative HQS ($g_z = 1.944$ and $|A_z| = 163 \times 10^{-4}$ $cm^{-1}$ [65]) that show a *cis*-octahedral geometry with $(O^-,N)$; $(O^-,N_{ax})$; $H_2O$ coordination. The calculated $\Delta G^{calcd}_{aq}$ and $A^{calcd}_z$, −17.3 kcal $mol^{-1}$ and $-161.2 \times 10^{-4}$ $cm^{-1}$, respectively, support the high stability of this species and its EPR parameters. Its stoichiometry is $[VO(HL^6)_2]$ and, after the deprotonation of the phenolic –OH, gives $[VO(HL^6)(L^6)]^-$, (see the concentration distribution curves in **Fig. S6.b**). Notably, the resonances of **III** coincide with those of $[VO(HQS)_2(H_2O)]^{2-}$ (**V** in Fig. 7). Moreover, the EPR spectrum in the mixture DMSO/$H_2O$ (v/v) 80/20 is superimposable with that of the solid $[VO(HL^6)_2]$ (**6**) dissolved in DMSO (Fig. 8), confirming the assignment. It should be noted in the solid phase the formation of neutral species is favoured compared to the behaviour in solution. The presence of a minor amount of the isomer with $(O^-,N)$; $(O^-_{ax},N)$; $H_2O$ coordination cannot be excluded. It is less stable than the other isomer with coordination $(O^-,N)$; $(O^-,N_{ax})$; $H_2O$ ($\Delta G^{calcd}_{aq} = -8.0$ *vs.* −17.3 kcal $mol^{-1}$) and $|A_z|^{calcd}$ should be larger (164.6 *vs.* 161.2 × $10^{-4}$ $cm^{-1}$) (Fig. 9).

Above pH 9 (Fig. 9), the minor species **IV** is detected with $g_z = 1.954$ and $|A_z| = 157.3 \times 10^{-4}$ $cm^{-1}$. This may be the mono-hydroxido species with formula $[VO(HL^6)(L^6)(OH)]^{2-}$ formed after the deprotonation of the equatorial $H_2O$ in $[(VO(HL^6)_2]/[VO(HL^6)(L^6)]^-$. The resonances of **IV** coincide with those of the mono-hydroxido complex of HQS (**VI** in Fig. 7). It should be noted that this is the pH range where the non-coordinating phenolic OH group of $L^6$ also dissociates, although the EPR parameters are assumed to be insensitive to this process.

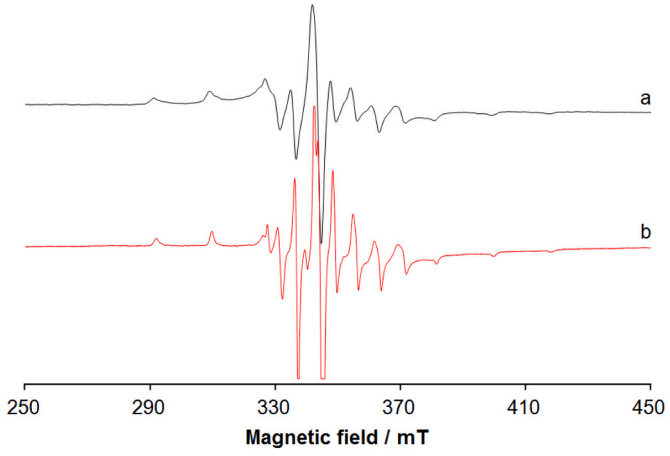


**Fig. 8.** X-band anisotropic EPR spectra recorded at 100-120 K on (a) $[VO(HL^6)_2]$ dissolved in DMSO and (b) the system containing $[V(IV)OSO_4{\cdot}3H_2O]$ and $L^6$ (molar ratio 1:1 and V(IV)O concentration 1.0 mM) in a mixture DMSO/$H_2O$ 80/20 (v/v) at pH 8.10.

The behaviour of $L^4$ ligand is significantly different, mainly at basic pH range (Fig. 10). As a function of pH, the formation of the species, with $M_I = 7/2$ resonances indicated with **I-V**, is detected. **I** is the mono-chelated complex with formula $[VO(HL^4)]^+$, coordination mode of 8-hydroxyquinoline $(N,O^-)$ and $g_z = 1.941$ and $|A_z| = 170.2 \times 10^{-4}$ $cm^{-1}$; **II** is the species with composition $[VO(H_2L^4)]^{2+}$, donor set $(N^1_{im}$, CO) and $g_z = 1.944$ and $|A_z| = 168.2 \times 10^{-4}$ $cm^{-1}$; **III** is the bis-chelated complex, similar to 8-hydroxyquinoline, with formula $[VO(HL^4)_2]$ and coordination mode $(O^-,N)$; $(O^-,N_{ax})$; $H_2O$, and with $g_z = 1.948$ and $|A_z| = 164.2 \times 10^{-4}$ $cm^{-1}$.

Above pH 9.5–10.0, two additional species, **IV** and **V**, different when compared with those of $L^6$, were detected. The attribution is confirmed examining the low field range of the anisotropic EPR spectra shown in **Fig. S7**. Species **IV** has $g_z = 1.944$ and $|A_z| = 167.1 \times 10^{-4}$ $cm^{-1}$; this constant can be compared with $A^{calcd}_z$ of $-166.9 \times 10^{-4}$ $cm^{-1}$ predicted for the complex $[VO(L^6)]$ formed upon the deprotonation of the benzohydrazide-NH group with a (5 + 6) chelate ring and $(O^-$, N, $N^2_{im})$; $H_2O$ coordination. For this complex $\Delta G^{calcd}_{aq}$ is −7.7 kcal $mol^{-1}$, that supports its stability. Moreover, at pH around 10, the vanadium complex **V** appears in solution; its spin Hamiltonian parameters are $g_z = 1.931$ and $|A_z| = 128.8 \times 10^{-4}$ $cm^{-1}$. Such small values of *g* and *A* are not typical for V(IV)O species and are attributed to non-oxido V(IV) species [58,69]. For this complex, which coexists with $[VO(L^4)]$ and is not detected by UV–Vis spectrophotometric titrations due to the different conditions used compared to EPR measurements, the ligand should be in the doubly deprotonated form and at least three isomers should be possible: one with (5 + 5) chelate rings, another with (5 + 6) and the third one with (6 + 6). To clarify the possible formation of this species, the three structures were optimized, and the spin Hamiltonian parameters were calculated at the level of theory B2PLYP/VTZ that allows to predict the value of $A_i$ for non-oxido V(IV) species with a mean absolute percent deviation (MAPD) in the range 3–4% [58]. The best values of $\Delta G^{calcd}_{aq}$ and $A^{exptl}_z$ were obtained for the (6 + 6) and (5 + 6) coordination mode and 2 × $(O^-,N,N^2_{im})$ and $(O^-,N,N^1_{im})$; $(O^-,N,N^2_{im})$ donor sets. The simulated structures are shown in Fig. 11 and the computed $\Delta G_{aq}$ energy and *A* values are listed in Table 5.

The reasons of the different behaviour of the methyl $(L^4)$ and hydroxyl $(L^6)$ derivatives are not clear. The EPR results justify the behaviour of $L^4$ and $L^6$ in the solid state, where $L^4$ forms the 1:1 species $[VO(L^4)]$ (**4**) and $L^6$ the 1:2 complex $[VO(HL^6)_2]$ (**6**); in particular, the EPR spectroscopy reveals that for $L^4$ the binding mode $(O^-,N,N^2_{im})$ is possible, while for $L^6$ it is not. This difference could be related to the different conformation of $L^4$ and $L^6$, detected also by $^1H$ NMR, but it is plausible to suppose that the solvation energy diversely stabilizes the complexes.

### 3.7. Interaction with biomolecules

The prepared V(IV)O-complexes were tested for their ability to interact with the genetic material, DNA, and bovine serum albumin, BSA, by spectroscopic methods. $[VO(HL^5)_2]$ (**5**) revealed a strong induced circular dichroic band in the 300–360 nm range upon addition of BSA confirming the ability of the complex to bind to the chiral protein, as seen in **Fig. S8**. In these CD spectra weak bands at *ca.* 450 and 620 nm are also detected. Such type of charge transfer (at *ca.* 450 nm) and d-d bands (at *ca.* 620 nm) can only be explained by the formation of coordination bonds between V(IV)O and chiral amino acid side groups of the protein; in this binding one of the ligands of $[VO(HL)_2]$ should be lost, as previously confirmed for several other complexes [28,70–76]. Thus, we expect that the species that binds BSA is $[VO(HL^5)]$. Considering the previous reports on the binding of $V(IV)O^{2+}$ complexes with human serum albumin (HSA), it can be inferred that the residues candidates to interact with vanadium moieties are exposed histidines on the BSA surface, namely His105, His366, His509 [77–79]. The complexes were also tested using a DNA intercalation assay. CD measurements did not confirm any binding to DNA and/or changes in the degree of

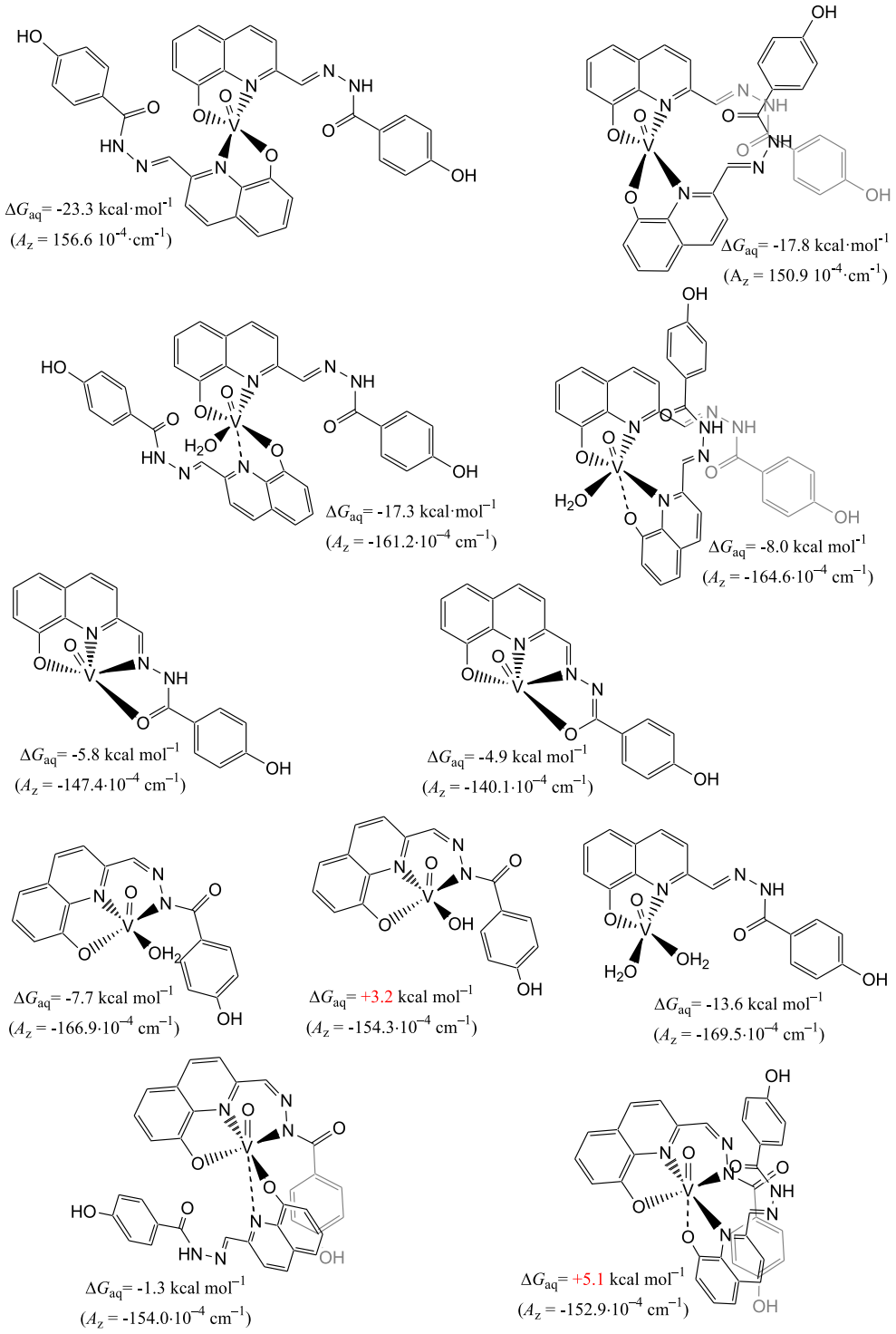


**Fig. 9.** Computed Gibbs energy values (B3LYP-D3/BS2 in SMD continuum model for water) and $A_z$ (BHandHLYP/6-311g+(d)) for the possible V(IV)O-complexes of $L^6$. It must be noted that other possible coordination modes are not reported since they i) present high formation energy and ii) do not correspond to energy minima and evolve towards one of the reported structures (see **Scheme S3**).

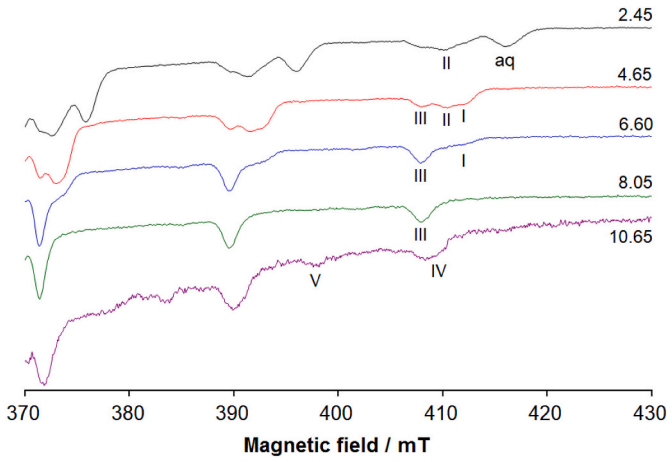


**Fig. 10.** High field region of the X-band anisotropic EPR spectra recorded as a function of pH at *ca.* 120 K in a mixture DMSO/$H_2O$ 80/20 (v/v) containing [V(IV)$OSO_4$·$3H_2O$] and $L^4$ (molar ratio 1:1 and V(IV)O concentration 1.0 mM). With **I**, **II**, **III**, **IV**, and **V** the $M_I = 7/2$ resonances of $[VO(HL^4)]^+$, $[VO(H_2L^4)]^{2+}$, $[VO(HL^4)_2]/[VO(HL^4)(L^4)]^-$, $[VO(L^4)]$ and $[V(L^4)_2]$ species are indicated.

supercoiling. On the other hand, incubation with **2** and **3** relaxed the plasmid and increased the nicked circular form (Fig. 12). Pre-incubation of samples with $NaN_3$, a ROS scavenger, completely reversed this effect suggesting that free radicals formation, induced by the complexes, were responsible for the observed effect.

To understand whether this is the case in cells, we tested the ability of these complexes for ROS induction in two cancer cells of different origins – melanoma (A-375) and lung (A-549) –, via staining with dihydroethidium, which is a fluorogenic probe that is readily oxidized by radical oxygen species, emitting green fluorescence. Interestingly, all complexes induced ROS in cells, but **3** and **5** showed the highest level of induction, which is comparable to cisplatin (Fig. 13). Hence, cellular environment appears to play a critical role in how these complexes can damage DNA.

### 3.8. Cytotoxicity

All compounds, including the free ligands, were tested on both melanoma (A-375) and lung adenocarcinoma (A-549) cell lines, using seven different concentrations (0.78–50 μM). Cells were incubated with the drugs for 72 h and cell survival was measured via sulforhodamine B assay (**Fig. S9**). Interestingly, all complexes were dramatically more potent on A-375 cells than on A-549 cells. This is in line with what was reported in the literature for other vanadium complexes [80,81]. While this may be due to differences of the tissue origin, it may also reflect the underlying genetic mutations that these cell lines intrinsically exhibit. While the free ligands $L^1$, $L^3$, $L^5$ and $L^6$ exhibited some toxicity on A-375 cells, the V-complexes of the same ligands proved to be more effective, in particular, **3** that showed the lowest $IC_{50}$ on both cell lines (Table 6). Moreover, all V(IV)O-complexes showed higher cytotoxicity than cisplatin, the positive control, in malignant melanoma cancer cells. Hence, all compounds resulted in loss of cell survival, albeit with varying efficiencies.

### 3.9. Mechanisms of cell death

The mode of cell death was examined through two different assays that help distinguish whether cells die from apoptosis or other forms of cell death. We initially evaluated flipping of phosphatidylserines to the outer leaflet of the plasma membrane through Annexin V staining. As phosphatidylserines usually face the cytoplasm, their presence on the outer membrane is an indication of apoptosis, a commonly used marker. Cells were co-stained with 7-AAD, a DNA stain, which helps to distinguish necrotic cell death. Our results showed that there was significant induction in Annexin V staining in A-375 cells, either at comparable levels or higher than the control compound, cisplatin (**Fig. S10** and Fig. 14). Consistent with cell viability experiments, A-549 cells were less sensitive to all the complexes, despite their responsiveness to cisplatin (Fig. 14b and **Fig. S11**). Moreover, similar to our observations on cell viability, **3** exhibited the highest increase in Annexin V staining and was effective even on A-549 cells. All complexes, except **2**, exhibited better efficacy than cisplatin in A-375 cells, but not in A-549 cells (Fig. 14 and **Fig. S11**).

To confirm that the main form of cell death was apoptosis, activation of caspases, which are essential proteases that cleave cellular proteins during programmed cell death, was evaluated in both cell lines. Once

**Table 5**
Computed $\Delta G_{aq}$ energy values (B3LYP-D3/BS2 in SMD continuum model for water) and $A$ values (B2PLYP/VTZ) for the three possible isomers of the non-oxido V(IV)-complex $V(L^4)_2$.

| Chelate cycles | $\Delta G_{aq}^{calcd}$[a] | $A_x^{calcd}$[b] | $A_y^{calcd}$[b] | $A_z^{calcd}$[b] | $A_z^{exptl}$[b] | PD ($A_z$) |
|---|---|---|---|---|---|---|
| 6 + 6[c] | 0.0 | −10.3 | −47.4 | −122.5 | −128.8 | −4.9 |
| 5 + 6[d] | 0.2 | −5.5 | −37.8 | −115.2 | −128.8 | −10.6 |
| 5 + 5[e] | 13.0 | −25.8 | −32.5 | −113.5 | −128.8 | −11.9 |

[a] Values in kcal $mol^{-1}$ and referred at (6 + 6) complex taken as a reference.
[b] Values in $10^{-4}$ $cm^{-1}$.
[c] Coordination 2 × ($O^-$,N,$N^2_{im}$).
[d] Coordination ($O^-$,N,$N^1_{im}$); ($O^-$,N,$N^2_{im}$).
[e] Coordination 2 × ($O^-$, N,$N^1_{im}$).

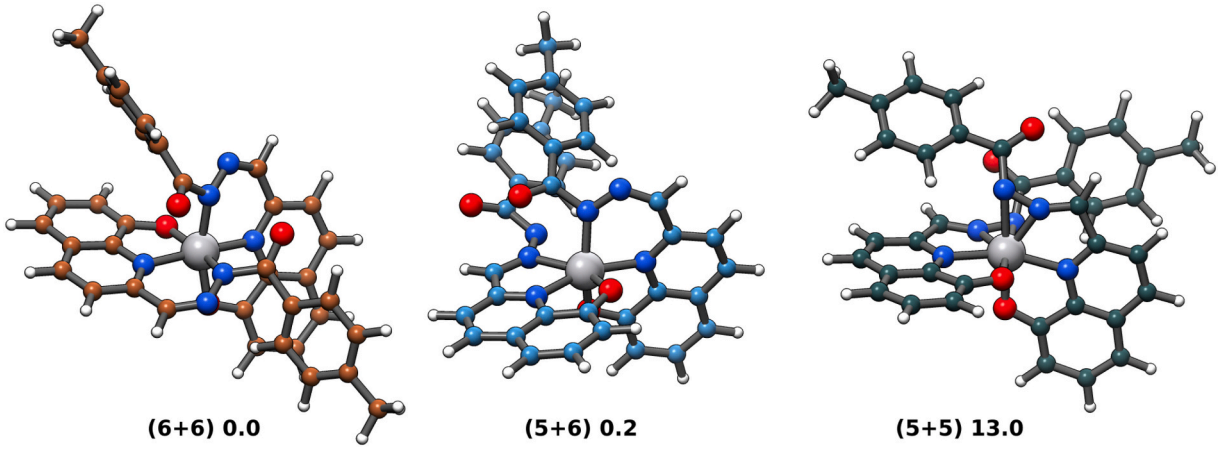


**Fig. 11.** DFT optimized structure of the complex $[V(L^4)_2]$. Relative $\Delta G$ values computed at B3LYP-D3/BS2 level are reported in kcal $mol^{-1}$.

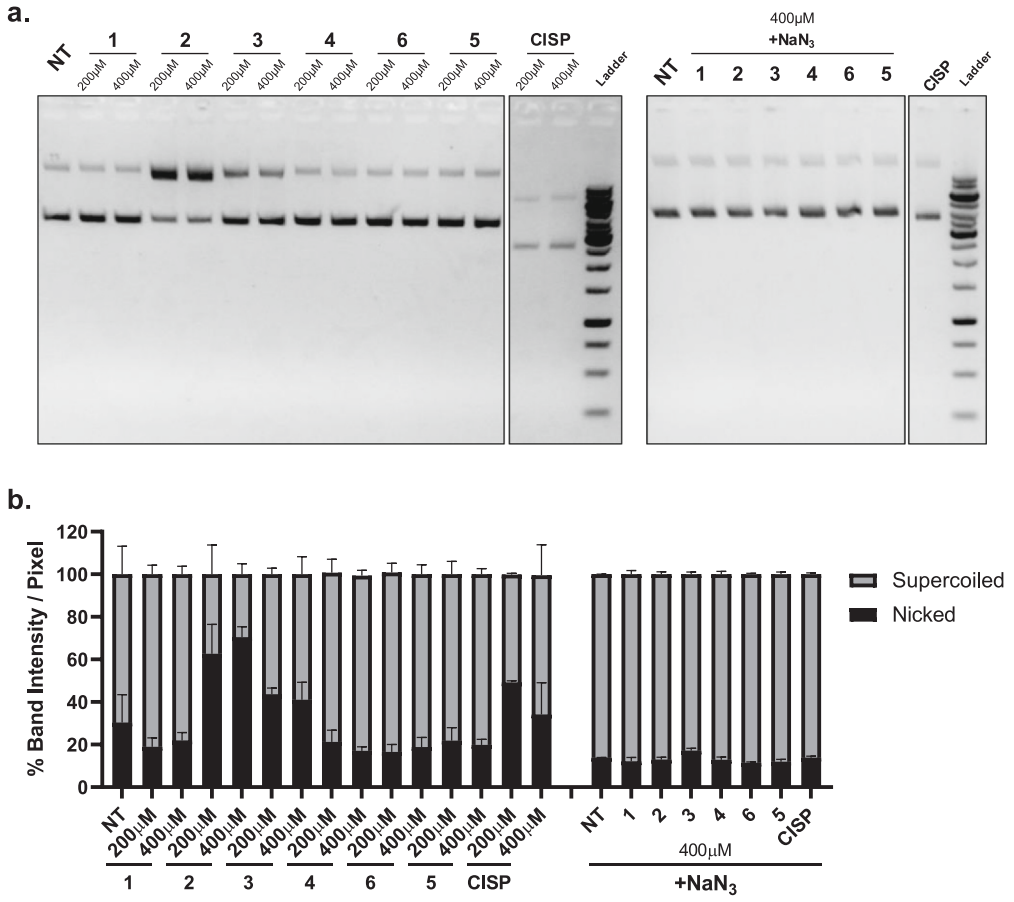


**Fig. 12.** DNA intercalation assay: plasmid DNA was incubated with different concentrations (200, 400 μM) of V(IV)O-complexes **1**–**6** and cisplatin (CISP) for 24 h at room temperature. $NaN_3$ was used as a ROS scavenger. The intensity of the DNA bands in each lane was quantified and represented as mean ± StDev ($n = 2$) for nicked circular and super coiled. **a)** Representative agarose gel electrophoresis images. **b)** Quantification of gels by Image J Software.

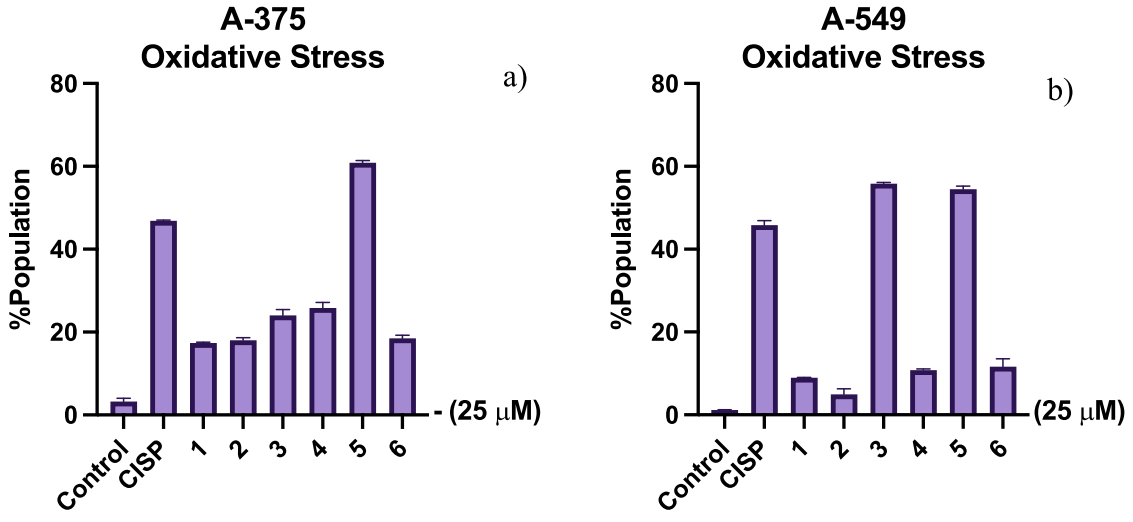


**Fig. 13.** Detection of ROS in cells: A-375 (a) and A-549 (b). Cells were treated with V(IV)O-complexes **1–6** and cisplatin (CISP) for 48 h and stained with dihydroethidium for the detection of ROS in cellular environment. The graphs show (%) population of ROS (+) cells.

**Table 6**
$IC_{50}$ values of free ligands $L^1$-$L^6$ and vanadium complexes **1–6** in comparison to the positive control compound cisplatin (μM ± standard deviation) on A-375 and A-549 cell lines, after incubation for 72 h.

| $IC_{50}$ concentration (μM ± StDev) | | | | | | | |
|---|---|---|---|---|---|---|---|
| A-375 | | | | A-549 | | | |
| **1** | 4.1 ± 0.5 | $L^1$ | 12.3 ± 0.5 | **1** | >50 | $L^1$ | >50 |
| **2** | 5.5 ± 0.2 | $L^2$ | >50 | **2** | 50 ± 1 | $L^2$ | >50 |
| **3** | 2.4 ± 0.1 | $L^3$ | 23.9 ± 1.5 | **3** | 20.1 ± 0.1 | $L^3$ | >50 |
| **4** | 4.9 ± 0.2 | $L^4$ | >50 | **4** | 44 ± 1 | $L^4$ | >50 |
| **5** | 5.1 ± 0.1 | $L^5$ | 30.9 ± 0.3 | **5** | 46.6 ± 0.8 | $L^5$ | >50 |
| **6** | 6.3 ± 0.9 | $L^6$ | 21.2 ± 0.2 | **6** | 45 ± 2 | $L^6$ | 46.9 ± 0.8 |
| cisplatin | 11.2 ± 0.3 | | | cisplatin | 17 ± 3 | | |

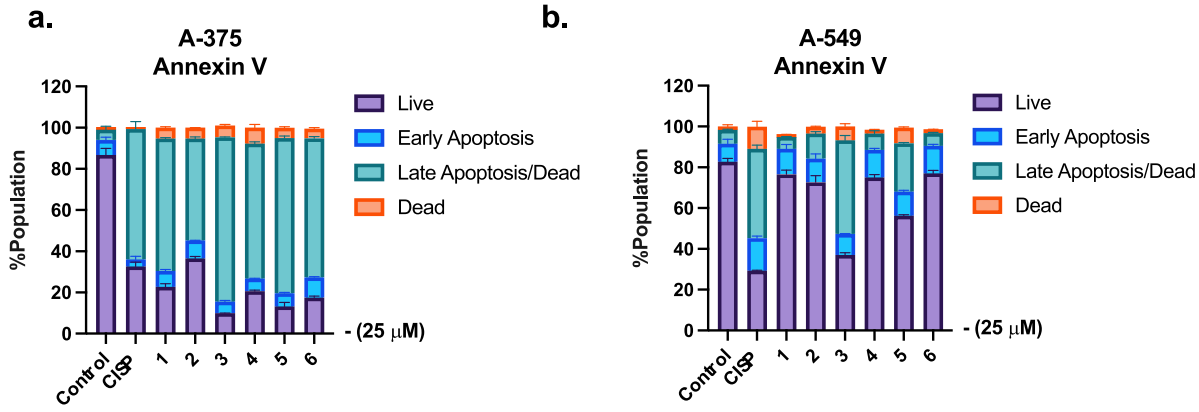


**Fig. 14.** Flow cytometric analysis on A-375 and A-549 cells using Annexin V and 7-AAD staining. A-375 and A-549 cells were exposed to V(IV)O-complexes **1–6** and cisplatin (CISP) (25 μM) for 48 h. Quantification and average of two replicates showing distribution of live, early-late apoptotic and dead cells. See also **Fig. S10**.

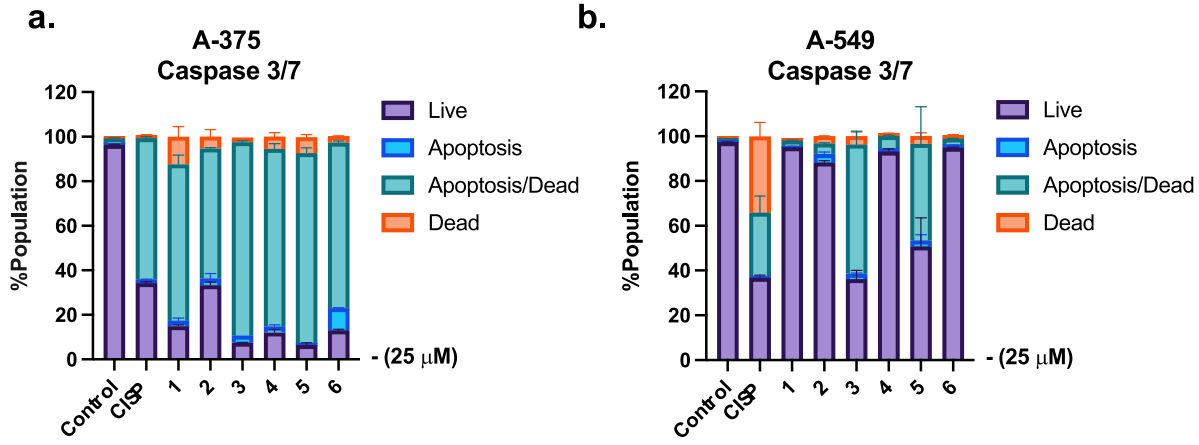


**Fig. 15.** Flow cytometry analysis on A-375 cells using Caspase 3/7 and 7-AAD staining. A-375 cells were exposed to V(IV)O-complexes **1–6** and cisplatin (CISP) (25 μM) for 48 h. Quantification and average of two replicates showing distribution of live, apoptotic and dead cells.

again, caspase3/7 activity was greatly induced upon treatment with all complexes in A-375 cells, supportive of apoptotic cell death (**Fig. S12** and Fig. 15). Consistent with our Annexin V data, **3** appeared as the most potent compound. A-549 cells were only mildly affected except for **3**, which was even more potent than cisplatin with >50% induction of apoptosis population (Fig. 15 and **Fig. S13**).

### *3.10. DNA damage in cells*

Since we observed relaxation of plasmid DNA, which is indicative of induction of single strand breaks (SSBs) in DNA intercalation experiments (Fig. 12) and an increase in ROS in cells (Fig. 13), we wished to examine whether we can detect breaks in cells. Since two SSBs that are close to each other will eventually form a double stranded break (DSB), we stained cells with γH2AX, which is a widely used marker for DSBs. Only A-375 cells were used, as they were the most responsive to drug treatment. There was induction of DSBs with all complexes, once again **3** being the highest among all (Fig. 16 and **S14**). Therefore, all complexes can induce ROS formation, which probably leads to SSBs followed by DSBs, potentially accounting for the observed apoptosis induced by these complexes.

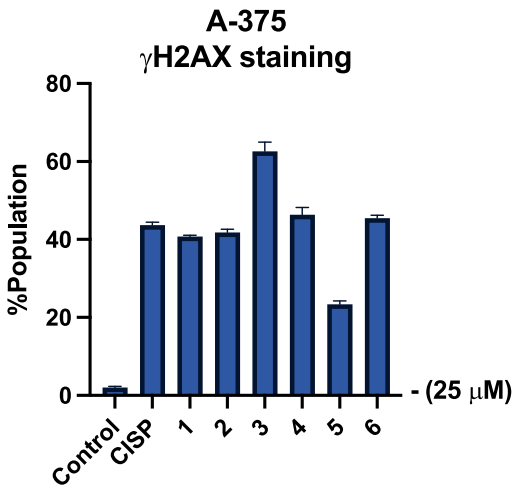


**Fig. 16.** Analysis of DSBs on A-375 cells. A-375 cells were exposed to V(IV)O-complexes **1–6** and cisplatin (CISP) (25 μM) for 48 h. Cells were stained with anti-phospho-Histone H2A.X (Ser139)-Alexa Fluor 555 and an anti-Histone H2A.X-PECy5 antibodies. Quantification of two repeats showing (%) population of γ-H2AX positive cells.

## 4. Conclusions

Four new benzylhydrazone ligand precursors were synthetized by condensation reactions as well as six new oxidovanadium(IV) complexes by reaction of the ligands with oxidovanadium(IV) ion. Complexes with both 1:1 and 1:2 metal to ligand stoichiometries were obtained, evidencing the coordinating versatility of the chosen ligand system. The proton dissociation constants of all ligand precursors, their lipophilicity and solubility at physiologic pH were determined. Compounds $L^1$-$L^5$ have three dissociable protons: OH, quinolinium $NH^+$ and benzohydrazide NH, while $L^6$ has an additional phenolic OH. The most acidic p$K_a$ belongs to the quinolinium $NH^+$, while p$K_{a2}$ and p$K_{a3}$ to the hydroxyl and the benzohydrazide NH moieties, respectively. Thus, $L^1$-$L^5$ are present in solution in their neutral $H_2L$ form at physiological pH but their thermodynamic solubility ($S_{7.4}$) at this pH and 25 °C is fairly low (< 4 μM).

Solution characterization of the V(IV)O-complexes was made by both spectrophotometric titrations (in the μM range) and EPR measurements (in the mM range) for systems with $L^4$ and $L^6$, and supported by DFT calculations. These studies evidenced the complexity of these systems, in which the ligands' conformation and solvation free energy certainly play key roles, since different species are found for both systems in solution, corroborating the different stoichiometries found in solid state for complexes **4** and **6**. Mono and bis complexes were found (as well as a non-oxido V(IV) species for $L^4$ in the highly basic pH). Different binding modes are proposed for $L^4$ and $L^6$, namely for the [VO(L)] species due to the different protonation scheme of the two ligand precursors and their preferential conformation.

All complexes appeared to be cytotoxic for cancer cells, albeit with varying efficiencies in cell lines of different origins. While this may be due to the different tissues the cells were isolated from, it most likely reflects the varying genetic backgrounds. Among all, complex **3** was the most potent compound on both cell lines, which was more efficient than the clinically used benchmark drug, cisplatin. The fact that A-549 cells responded both to cisplatin and **3**, the difference in survival cannot be attributed to DNA damage repair capacity of these cells. The actual mechanism of action and deeper evaluation of these cells are required to resolve the difference. Notwithstanding, it is not likely that the V(IV)O complexes maintain their integrity inside cells [72,73].

It has been widely shown [82,83] that the presence of fluorine increases the biological activity of a compound, when compared with unsubstituted related compounds, and here we observe the same effect since complex **3** contains the F-substituted ligand. Fluorine is considered the second "favourite" heteroatom, following nitrogen, for drug design, since its incorporation often brings pharmacologically beneficial effects. Several reasons have been used to explain this, namely its capacity to enhance metabolic stability and its effect in protein binding affinity and selectivity at the molecular level.

The mechanism of action of the complexes was through ROS induced DNA damage, which was shown not only biochemically, but also in cells through dihydroethidium staining, and formation of γH2AX staining. The form of cell death was determined to be apoptosis since there was an increase in both Annexin V staining and caspase activity. Overall, **3** is a promising compound, which holds promise for anticancer therapy.

## CRediT authorship contribution statement

**Nádia Ribeiro:** Investigation, Formal analysis, Writing – original draft. **Ipek Bulut:** Investigation, Formal analysis, Writing – original draft. **Vivien Pósa:** Investigation, Formal analysis. **Baris Sergi:** Investigation, Formal analysis. **Giuseppe Sciortino:** Investigation, Formal analysis. **João Costa Pessoa:** Validation, Writing – review & editing. **Luisa B. Maia:** Investigation, Formal analysis. **Valeria Ugone:** Investigation, Formal analysis. **Eugenio Garribba:** Formal analysis, Validation, Supervision, Writing – review & editing. **Éva A. Enyedy:** Formal analysis, Validation, Supervision, Writing – review & editing. **Ceyda Acilan:** Conceptualization, Validation, Supervision, Writing – review & editing. **Isabel Correia:** Conceptualization, Funding acquisition, Supervision, Writing – review & editing.

## Declaration of Competing Interest

The authors declare that they have no known competing financial interests or personal relationships that could have appeared to influence the work reported in this paper.

## Data availability

Data will be made available on request.

## Acknowledgements

This work was supported by Centro de Química Estrutural, which is financed by national funds from Fundação para a Ciência e Tecnologia (FCT), projects UIDB/00100/2020, UIDP/00100/2020 and LA/P/0056/2020, and Programa Operacional Regional de Lisboa 2020. We also thank project PTDC/QUI-QIN/0586/2020 and N. Ribeiro acknowledges FCT for SFRH/BD/135797/2018 grant. The Portuguese NMR and Mass spectrometry IST-UL are acknowledged for the access to the equipment. This work was supported by the Portuguese-Hungarian Scientific & Technological CooperationTÉT-PT-2018-00002, ÚNKP-21-3-SZTE-455 (to V. Pósa) New National Excellence Program Ministry of Human Capacities. The support of the 'Lendület' Programme (ELKH, LP2019-6/2019) and the COST ActionCA18202, NECTAR-Network for Equilibria and Chemical Thermodynamics Advanced Research is also acknowledged. This work was also supported by Koç University School of Medicine (KUSOM) and the authors gratefully acknowledge use of the services and facilities of the Koç University Research Center for Translational Medicine (KUTTAM), funded by the Presidency of Turkey, Presidency of Strategy and Budget. The content is solely the responsibility of the authors and does not necessarily represent the official views of the Presidency of Strategy and Budget. G. Sciortino, V. Ugone, E. Garribba thank Fondazione di Sardegna (grant FdSGarribba2017) and Regione Autonoma della Sardegna (grant RASSR79857); G. Sciortino also thanks MICINN' Juan de la Cierva program, FJC2019-039135-I for the financial support. L. Maia thanks the Associate Laboratory for Green Chemistry - LAQV, which is financed by national funds from Fundação

para a Ciência e a Tecnologia, MCTES (FCT/MCTES; UIDB/50006/2020 and UIDP/50006/2020).

## Appendix A. Supplementary data

Supplementary data to this article can be found online at https://doi.org/10.1016/j.jinorgbio.2022.111932.

## References


[1] A.R. Joaquim, M.P. Gionbelli, G. Gosmann, A.M. Fuentefria, M.S. Lopes, S. F. Andrade, J. Med. Chem. 64 (2021) 16349–16379.
[2] C.M. Darby, C.F. Nathan, J. Antimicrob. Chemother. 65 (2010) 1424–1427.
[3] W.Q. Ding, B.L. Liu, J.L. Vaught, H. Yamauchi, S.E. Lind, Cancer Res. 65 (2005) 3389–3395.
[4] B. Pippi, W. Lopes, P. Reginatto, F.É.K. Silva, A.R. Joaquim, R.J. Alves, G. P. Silveira, M.H. Vainstein, S.F. Andrade, A.M. Fuentefria, Saudi Pharm. J. 27 (2019) 41–48.
[5] S.M. Zhai, L. Yang, Q.C. Cui, Y. Sun, Q.P. Dou, B. Yan, J. Biol. Inorg. Chem. 15 (2010) 259–269.
[6] V. Oliveri, M.L. Giuffrida, G. Vecchio, C. Aiello, M. Viale, Dalton Trans. 41 (2012) 4530–4535.
[7] V. Oliveri, G. Vecchio, Eur. J. Med. Chem. 120 (2016) 252–274.
[8] D. Rogolino, A. Cavazzoni, A. Gatti, M. Tegoni, G. Pelosi, V. Verdolino, C. Fumarola, D. Cretella, P.G. Petronini, M. Carcelli, Eur. J. Med. Chem. 128 (2017) 140–153.
[9] V. Prachayasittikul, S. Prachayasittikul, S. Ruchirawat, V. Prachayasittikul, Drug Des. Dev. Ther. 7 (2013) 1157–1178.
[10] T. Le Bahers, C. Adamo, I. Ciofini, J. Phys. Chem. A 114 (2010) 5932–5939.
[11] H.C. Jiang, J.E. Taggart, X.X. Zhang, D.M. Benbrook, S.E. Lind, W.Q. Ding, Cancer Lett. 312 (2011) 11–17.
[12] A. Mitrović, J. Kos, Acta Biochim. Pol. 66 (2019) 521–531.
[13] R. Khan, H. Khan, Y. Abdullah, Q.P. Dou, Recent Pat. Anticancer Drug. Discov. 15 (2020) 14–31.
[14] Y.C. Liu, J.H. Wei, Z.F. Chen, M. Liu, Y.Q. Gu, K.B. Huang, Z.Q. Li, H. Liang, Eur. J. Med. Chem. 69 (2013) 554–563.
[15] Q.P. Qin, Z.F. Chen, J.L. Qin, X.J. He, Y.L. Li, Y.C. Liu, K.B. Huang, H. Liang, Eur. J. Med. Chem. 92 (2015) 302–313.
[16] I.E. León, P. Díez, E.J. Baran, S.B. Etcheverry, M. Fuentes, Metallomics 9 (2017) 891–901.
[17] K. Choroba, L.R. Raposo, J. Palion-Gazda, E. Malicka, K. Erfurt, B. Machura, A. R. Fernandes, Dalton Trans. 49 (2020) 6596–6606.
[18] J. Palion-Gazda, A. Luz, L.R. Raposo, K. Choroba, J.E. Nycz, A. Bieńko, A. Lewińska, K. Erfurt, P.V. Baptista, B. Machura, A.R. Fernandes, L.S. Shul'pina, N. S. Ikonnikov, G.B. Shul'pin, Molecules 26 (2021) 6364.
[19] I. Correia, P. Adão, S. Roy, M. Wahba, C. Matos, M.R. Maurya, F. Marques, F. R. Pavan, C.Q.F. Leite, F. Avecilla, J. Costa Pessoa, J. Inorg. Biochem. 141 (2014) 83–93.
[20] H. Zhang, R. Thomas, D. Oupicky, F. Peng, J. Biol. Inorg. Chem. 13 (2008) 47–55.
[21] F. Xie, H.W. Cai, F.Y. Peng, J. Biol. Inorg. Chem. 23 (2018) 949–956.
[22] Ł. Popiołek, A. Biernasiuk, Chem. Biodivers. 14 (2017), e1700075.
[23] B. Yadagiri, U.D. Holagunda, R. Bantu, L. Nagarapu, V. Guguloth, S. Polepally, N. Jain, Bioorg. Med. Chem. Lett. 24 (2014) 5041–5044.
[24] F.R. Pavan, S.M.P.I. Da, S.R. Leite, V.M. Deflon, A.A. Batista, D.N. Sato, S. G. Franzblau, C.Q. Leite, Eur. J. Med. Chem. 45 (2010) 1898–1905.
[25] Ł. Popiołek, Int. J. Mol. Sci. 22 (2021) 9389.
[26] P.C. Sharma, D. Sharma, A. Sharma, N. Saini, R. Goyal, M. Ola, R. Chawla, V. K. Thakur, Mater. Today Chem. 18 (2020), 100349.
[27] T. Nasr, S. Bondock, M. Youns, Eur. J. Med. Chem. 76 (2014) 539–548.
[28] A. Banerjee, S.P. Dash, M. Mohanty, D. Sanna, G. Sciortino, V. Ugone, E. Garribba, H. Reuter, W. Kaminsky, R. Dinda, J. Inorg. Biochem. 199 (2019), 110786.
[29] M. Albrecht, O. Osetska, R. Fröhlich, Dalton Trans. (2005) 3757–3762.
[30] Y.-C. Liu, Z.-Y. Yang, Eur. J. Med. Chem. 44 (2009) 5080–5089.
[31] Y.-C. Liu, Z.-Y. Yang, J. Inorg. Biochem. 103 (2009) 1014–1022.
[32] Y.-C. Liu, Z.-Y. Yang, J. Organomet. Chem. 694 (2009) 3091–3101.
[33] Y.-C. Liu, Z.-Y. Yang, Inorg. Chem. Commun. 12 (2009) 704–706.
[34] Y.-C. Liu, Z.-Y. Yang, Biometals 22 (2009) 733–751.
[35] Y.-C. Liu, Z.-Y. Yang, J. Biochem. 147 (2009) 381–391.
[36] Y. Liu, X. Jiang, Z. Yang, X. Zheng, J. Liu, T. Zhou, Appl. Spectrosc. 64 (2010) 980–985.
[37] Y. Liu, Z. Yang, K. Zhang, Y. Wu, J. Zhu, T. Zhou, Aust. J. Chem. 64 (2011) 345–354.
[38] I. Nagypál, I. Fábián, Inorg. Chim. Acta 61 (1982) 109–113.
[39] M. Hassani, W. Cai, D.C. Holley, J.P. Lineswala, B.R. Maharjan, G.R. Ebrahimian, H. Seradj, M.G. Stocksdale, F. Mohammadi, C.C. Marvin, J.M. Gerdes, H.D. Beall, M. Behforouz, J. Med. Chem. 48 (2005) 7733–7749.
[40] H.M. Irving, M.G. Miles, L.D. Pettit, Anal. Chim. Acta 38 (1967) 475–488.
[41] L. Zékány, I. Nagipál, Computational Methods for the Determination of Formation Constants, Springer, US, Boston, MA, 1985, pp. 291–353.
[42] E. Kiss, K. Kawabe, A. Tamura, T. Jakusch, H. Sakurai, T. Kiss, J. Inorg. Biochem. 95 (2003) 69–76.
[43] L. Vilas Boas, J. Costa Pessoa, Vanadium, in: G. Wilkinson, R.D. Gillard, J. A. McCleverty (Eds.), Comprehensive Coordination Chemistry vol. 3, Pergamon, Oxford, 1987, pp. 453–583.
[44] J. Costa Pessoa, J. Inorg. Biochem. 147 (2015) 4–24.
[45] D. Sanna, E. Garribba, G. Micera, J. Inorg. Biochem. 103 (2009) 648–655.
[46] M.J. Frisch, G.W. Trucks, H.B. Schlegel, G.E. Scuseria, M.A. Robb, J.R. Cheeseman, G. Scalmani, V. Barone, G.A. Petersson, H. Nakatsuji, X. Li, M. Caricato, A. V. Marenich, J. Bloino, B.G. Janesko, R. Gomperts, B. Mennucci, H.P. Hratchian, J. V. Ortiz, A.F. Izmaylov, J.L. Sonnenberg, F. Ding Williams, F. Lipparini, F. Egidi, J. Goings, B. Peng, A. Petrone, T. Henderson, D. Ranasinghe, V.G. Zakrzewski, J. Gao, N. Rega, G. Zheng, W. Liang, M. Hada, M. Ehara, K. Toyota, R. Fukuda, J. Hasegawa, M. Ishida, T. Nakajima, Y. Honda, O. Kitao, H. Nakai, T. Vreven, K. Throssell, J.A. Montgomery Jr., J.E. Peralta, F. Ogliaro, M.J. Bearpark, J. J. Heyd, E.N. Brothers, K.N. Kudin, V.N. Staroverov, T.A. Keith, R. Kobayashi, J. Normand, K. Raghavachari, A.P. Rendell, J.C. Burant, S.S. Iyengar, J. Tomasi, M. Cossi, J.M. Millam, M. Klene, C. Adamo, R. Cammi, J.W. Ochterski, R.L. Martin, K. Morokuma, O. Farkas, J.B. Foresman, D.J. Fox, Gaussian 16 Rev. B.01, Gaussian, Inc., Wallingford, CT, 2016.
[47] S. Grimme, J. Antony, S. Ehrlich, H. Krieg, J. Chem. Phys. 132 (2010), 154104.
[48] A.W. Ehlers, M. Böhme, S. Dapprich, A. Gobbi, A. Höllwarth, V. Jonas, K.F. Köhler, R. Stegmann, A. Veldkamp, G. Frenking, Chem. Phys. Lett. 208 (1993) 111–114.
[49] A.V. Marenich, C.J. Cramer, D.G. Truhlar, J. Phys. Chem. B 113 (2009) 6378–6396.
[50] F. Weigend, R. Ahlrichs, Phys. Chem. Chem. Phys. 7 (2005) 3297–3305.
[51] V.S. Bryantsev, M.S. Diallo, W.A. Goddard, J. Phys. Chem. B112 (2008) 9709–9719.
[52] A. Cabré, G. Sciortino, G. Ujaque, X. Verdaguer, A. Lledós, A. Riera, Org. Lett. 20 (2018) 5747–5751.
[53] G. Micera, E. Garribba, J. Comput. Chem. 32 (2011) 2822–2835.
[54] D. Sanna, K. Varnágy, S. Timári, G. Micera, E. Garribba, Inorg. Chem. 50 (2011) 10328–10341.
[55] G. Sciortino, J.D. Marechal, I. Fabian, N. Lihi, E. Garribba, J. Inorg. Biochem. 204 (2020), 110953.
[56] F. Neese, ORCA – An Ab Initio, DFT and Semiempirical Program Package, Version 4.0, Max-Planck-Institute for Chemical Energy Conversion, Mülheim A. D. Ruhr, 2017.
[57] F. Neese, F. Wennmohs, U. Becker, C. Riplinger, J. Chem. Phys. 152 (2020), 224108.
[58] D. Sanna, G. Sciortino, V. Ugone, G. Micera, E. Garribba, Inorg. Chem. 55 (2016) 7373–7387.
[59] B. Sergi, I. Bulut, Y. Xia, Z.A.E. Waller, Y. Yildizhan, C. Acilan, R.M. Lord, Chem. Med. Chem. 16 (2021) 2402–2410.
[60] L.V. de Freitas, C.C.P. da Silva, J. Ellena, L.A.S. Costa, N.A. Rey, Spectrochim. Acta A Mol. Biomol. Spectrosc. 116 (2013) 41–48.
[61] P. Shah, L.F. Abadi, S. Gaikwad, D. Chaudhari, V. Kushwah, S. Jain, K.K. Bhutani, S. Kulkarni, I.P. Singh, ChemistrySelect 3 (2018) 10727–10731.
[62] É.A. Enyedy, O. Dömötör, E. Varga, T. Kiss, R. Trondl, C.G. Hartinger, B.K. Keppler, J. Inorg. Biochem. 117 (2012) 189–197.
[63] E.J. Baran, J. Coord. Chem. 43 (1998) 335–343.
[64] J. Costa Pessoa, M.J. Calhorda, I. Cavaco, I. Correia, M.T. Duarte, V. Felix, R. T. Henriques, M.F.M. Piedade, I. Tomaz, J. Chem. Soc. Dalton Trans. (2002) 4407–4415.
[65] E. Garribba, G. Micera, D. Sanna, E. Lodyga-Chruscinska, Inorg. Chim. Acta 348 (2003) 97–106.
[66] A. Rockenbauer, L. Korecz, Appl. Magn. Reson. 10 (1996) 29–43.
[67] G. Micera, E. Garribba, Eur. J. Inorg. Chem. 2010 (2010) 4697–4710.
[68] E. Lodyga-Chruscinska, G. Micera, E. Garribba, Inorg. Chem. 50 (2011) 883–899.
[69] A. Banerjee, S.P. Dash, M. Mohanty, G. Sahu, G. Sciortino, E. Garribba, M.F.N. N. Carvalho, F. Marques, J. Costa Pessoa, W. Kaminsky, K. Brzezinski, R. Dinda, Inorg. Chem. 59 (2020) 14042–14057.
[70] I. Correia, T. Jakusch, E. Cobbinna, S. Mehtab, I. Tomaz, N.V. Nagy, A. Rockenbauer, J. Costa Pessoa, T. Kiss, Dalton Trans. 41 (2012) 6477–6487.
[71] T. Jakusch, J. Costa Pessoa, T. Kiss, Coord. Chem. Rev. 255 (2011) 2218–2226.
[72] P. Nunes, I. Correia, I. Cavaco, F. Marques, T. Pinheiro, F. Avecilla, J. Costa Pessoa, J. Inorg. Biochem. 217 (2021), 111350.
[73] M.F.A. Santos, G. Sciortino, I. Correia, A.C.P. Fernandes, T. Santos-Silva, F. Pisanu, E. Garribba, J. Costa Pessoa, Chem. Eur. J. (2022), e2022000105.
[74] D. Sanna, V. Ugone, G. Micera, P. Buglyó, L. Bíró, E. Garribba, Dalton Trans. 46 (2017) 8950–8967.
[75] G. Sciortino, D. Sanna, V. Ugone, J.-D. Maréchal, M. Alemany-Chavarria, E. Garribba, New J. Chem. 43 (2019) 17647–17660.
[76] V. Ugone, D. Sanna, G. Sciortino, D.C. Crans, E. Garribba, Inorg. Chem. 59 (2020) 9739–9755.
[77] D. Sanna, V. Ugone, G. Sciortino, P. Buglyó, Z. Bihari, P.L. Parajdi-Losonczi, E. Garribba, Dalton Trans. 47 (2018) 2164–2182.
[78] G. Sciortino, D. Sanna, G. Lubinu, J.-D. Maréchal, E. Garribba, Chem. Eur. J. 26 (2020) 11316–11326.
[79] G. Sciortino, J.-D. Maréchal, E. Garribba, Inorg. Chem. Front. 8 (2021) 1951–1974.
[80] C. Rozzo, D. Sanna, E. Garribba, M. Serra, A. Cantara, G. Palmieri, M. Pisano, J. Inorg. Biochem. 174 (2017) 14–24.
[81] M. Pisano, C. Arru, M. Serra, G. Galleri, D. Sanna, E. Garribba, G. Palmieri, C. Rozzo, Metallomics 11 (2019) 1687–1699.
[82] C. Isanbor, D. O'Hagan, J. Fluor. Chem. 127 (2006) 303–319.
[83] K. Müller, C. Faeh, F. Diederich, Science 317 (2007) 1881–1886.